Article

Phase-Selective Epitaxy of Trigonal and Orthorhombic Bismuth Thin Films on Si (111)

Abdur Rehman Jalil [1,2,3,*], Xiao Hou [2,4], Peter Schüffelgen [1,2], Jin Hee Bae [1], Elmar Neumann [5], Gregor Mussler [1], Lukasz Plucinski [4] and Detlev Grützmacher [1,2,3]

1   Peter Grünberg Institute (PGI-9), Forschungszentrum Jülich, 52425 Jülich, Germany
2   JARA-FIT (Fundamentals of Future Information Technology), Jülich-Aachen Research Alliance, Forschungszentrum Jülich and RWTH Aachen University, 52425 Jülich, Germany
3   Peter Grünberg Institute (PGI-10), JARA-Green IT, Forschungszentrum Jülich, 52425 Jülich, Germany
4   Peter Grünberg Institute (PGI-6), Forschungszentrum Jülich, 52425 Jülich, Germany
5   Helmholtz Nano Facility (HNF), Forschungszentrum Jülich, 52425 Jülich, Germany
*   Correspondence: a.jalil@fz-juelich.de; Tel.: +49-176-70339392

Abstract: Over the past three decades, the growth of Bi thin films has been extensively explored due to their potential applications in various fields such as thermoelectrics, ferroelectrics, and recently for topological and neuromorphic applications, too. Despite significant research efforts in these areas, achieving reliable and controllable growth of high-quality Bi thin-film allotropes has remained a challenge. Previous studies have reported the growth of trigonal and orthorhombic phases on various substrates yielding low-quality epilayers characterized by surface morphology. In this study, we present a systematic growth investigation, enabling the high-quality growth of Bi epilayers on Bi-terminated Si (111) 1×1 surfaces using molecular beam epitaxy. Our work yields a phase map that demonstrates the realization of trigonal, orthorhombic, and pseudocubic thin-film allotropes of Bi. In-depth characterization through X-ray diffraction (XRD) techniques and scanning transmission electron microscopy (STEM) analysis provides a comprehensive understanding of phase segregation, phase stability, phase transformation, and phase-dependent thickness limitations in various Bi thin-film allotropes. Our study provides recipes for the realization of high-quality Bi thin films with desired phases, offering opportunities for the scalable refinement of Bi into quantum and neuromorphic devices and for revisiting technological proposals for this versatile material platform from the past 30 years.

Keywords: topological thin films; phase-change materials; structural transformation; phase-selective growth; molecular beam epitaxy; neuromorphic platform

1. Introduction

Bi is the heaviest ($Z = 83$) non-radioactive element that exhibits strong spin-orbit coupling [1,2] and as such, provides a unique and extremely versatile material platform. The strong spin-orbit coupling renders many Bi modifications topologically non-trivial [3–6], including higher-order topological insulator phase [7,8]. The thinnest of all topologically non-trivial modifications is Bismuthene [9,10]. Analogous to graphene, Bismuthene consists of a monolayer of Bi in a honeycomb lattice. This monolayer has been shown to be a quantum-spin-Hall (QSH) insulator with helical edge states and an inverted bandgap as large as 800 meV. According to the literature, not only Bismuthene, but also thin Bi layers (<1 nm) of trigonal (Bi_{TRIG}) and orthorhombic (Bi_{ORTH}) phases (Figure 1) exhibit a QSH phase, rendering them 2D topological insulators, too [11–14]. The difficulty of creating coalesced, phase-pure thin films of homogenous thickness below 1 nm, however, makes it impossible to provide the desired crystals for exploiting Bi-based 2D TIs for technological purposes in the field of quantum spintronics and topological quantum computation.
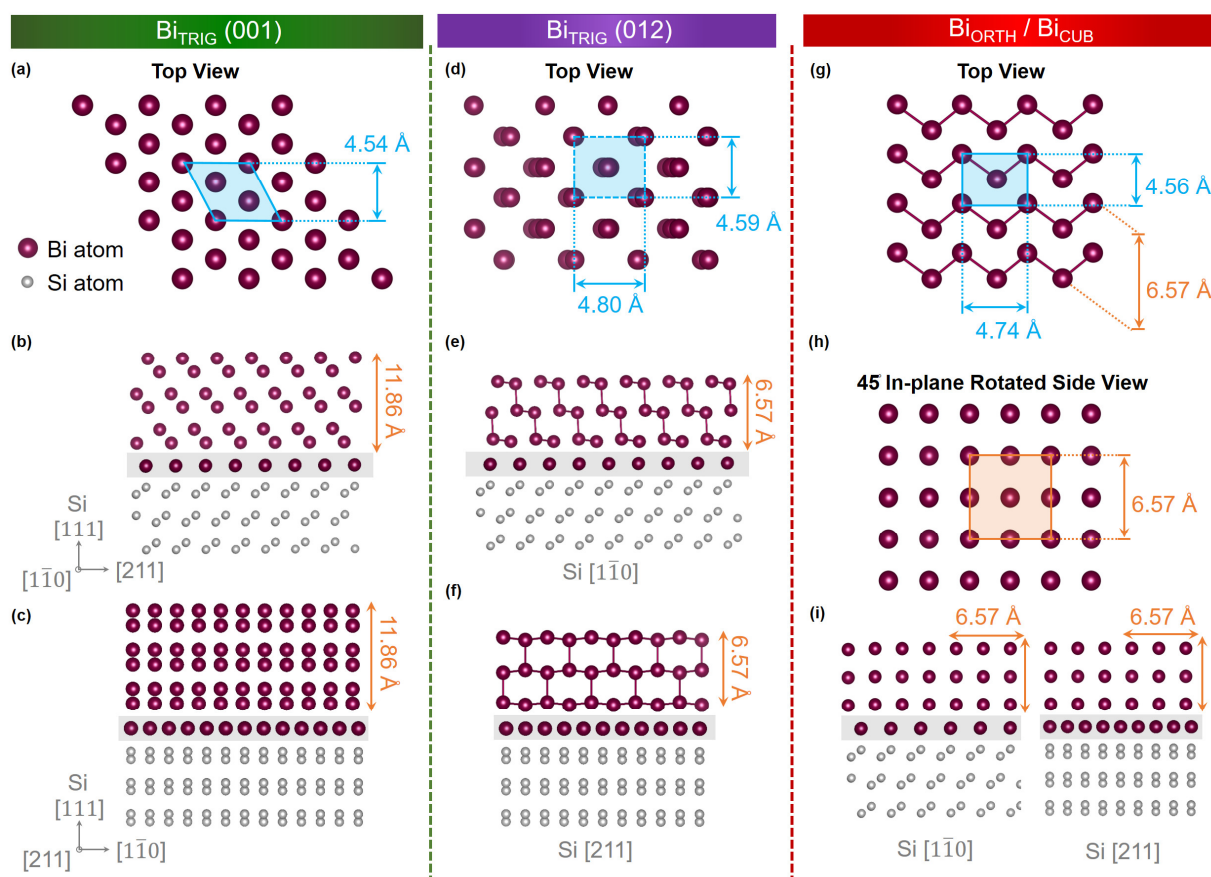
Figure 1. Crystal structure illustrations of Bismuth nanofilm allotropes. (**a**) Top surface view of Bi_{TRIG} (001) where the blue region highlights the 2D in-plane lattices, cross-sectional side view of one unit-cell thick epilayer of Bi_{TRIG} (001) along (**b**) Si $[1\bar{1}0]$ and (**c**) Si [211] projections. (**d**) Top surface view of Bi_{TRIG} (012) orientation having two monolayer thick film, cross-sectional side view of one unit-cell thick epilayer of Bi_{TRIG} (012) along (**e**) Si $[1\bar{1}0]$ and (**f**) Si [211] projections. (**g**) Top surface view of Bi_{ORTH} phase, (**h**) side view at 45 rotated plane, (**i**) cross-sectional side view of one unit-cell thick epilayer of Bi_{ORTH} (010) along Si $[1\bar{1}0]$ and Si [211] projections.

While Bismuthene comes with its own challenges, such as its restriction to SiC substrates, Bi_{ORTH} and Bi_{TRIG} have been successfully grown on top of HOPG [13,15], sapphire [16], InP (111) [14], glass [17], mica [18], and extensively on Si (111). While growing on Si (111) substrates, all reported growths were conducted on either $\sqrt{3} \times \sqrt{3} - \beta$ [19,20] or 7×7 [21–25] reconstructed surfaces. Both reconstructions facilitate epitaxy in the early stages of growth by providing a high density of nucleation sites; however, both result in an increased number of rotational domains with relatively small grain sizes, reducing the overall quality of epilayers [26–28]. Additionally, the maximum height before leaving the topological phase, approx. 0.8 nm for Bi_{TRIG} and 1.3 nm for Bi_{ORTH} phases, limits the realization of high-quality coalesced thin films in the 2D TI regime. Interestingly, the critical value of 1.3 nm in the Bi_{ORTH} phase is related to the amount of buckling in the epilayer. Hence, by finding a way to reduce the buckling, even thicker layers of Bi_{ORTH} might transform into the topological regime, opening an avenue to grow high-quality fully coalesced topological Bi thin films. As found in this study, the growth on Si (111) 1×1 offers unique possibilities in this regard.

Here, a systematic growth study of Bi epilayers, via molecular beam epitaxy on Si (111) $1 \times 1-$ Bi terminated surfaces was performed. The advantages of opting for the Si (111) 1×1 surface over 7×7 and $\sqrt{3} \times \sqrt{3} - \beta$ reconstructed surfaces are exemplified by the successful achievement of phase-pure epitaxy of Bi_{TRIG} (001) and Bi_{ORTH} (010) thin films with thicknesses up to 30 nm. Strikingly, the buckling in the orthorhombic phase on

1×1 reconstruction is highly reduced compared to 7×7 and $\sqrt{3} \times \sqrt{3} - \beta$, which moves the critical value for a cross-over toward the topologically trivial regime to a thickness of 9 nm.

Using systematic selection of growth parameters, a phase map is introduced where the optimum growth parameters for Bi_{TRIG} (001), Bi_{TRIG} (012) and Bi_{ORTH} (010) allotropes are identified. Previous studies have encountered challenges in distinguishing between different nanofilm allotropes of bismuth, leading to uncertainties in characterization. Thin films of some phases exhibit almost identical top surfaces, whereas they significantly differ in the in-plane structure. An overview of crystal structure, depicting the top and cross-sectional side-facets of all attained allotropes in this work, is presented in Figure 1, where the similarity between Bi_{TRIG} (012) and Bi_{ORTH} top-surfaces cannot be ignored. As most of the reported characterizations are based on top-surface investigations, including STM/STS [13,16,20,21,29], AFM [15] and LEED [22,27], the differentiation between various phases is challenging and somewhat vague. By conducting in-depth in-plane structural investigations on both single- and polycrystalline epilayers, this study offers a comprehensive understanding of domain alignment in different phases, effectively resolving any ambiguity in distinguishing between Bi_{TRIG} (012) and Bi_{ORTH} phases. Taking earlier reports on Bi nanofilm allotropes into account, several unsolved questions regarding the possibility of phase segregation, phase stability, phase transformation, and phase-dependent thickness limitations are systematically exploited and addressed in this study.

In addition to the opportunities this study creates for exploring topological devices, the optimized growth techniques developed in this research hold the potential to benefit a wide range of other fields as well. Topologically trivial Bi undergoes an electronic transition from a semimetal to a semiconductor through quantum confinement [30–32]. In its semiconducting regime, Bi can be exploited in quantum sensors [33] or used as a ferroelectric [15]. Additionally, due to its poor thermal stability, Bi is a suitable candidate for phase-change applications where the crystalline Bi film can be transformed into an amorphous state with relatively low applied energy [34]. The thermal instability of Bi_{TRIG} and ferroelectric attributes of Bi_{ORTH} designate Bi, in either phase, as one of the most promising candidates for low-power neuromorphic applications. Overall, we are confident that the results of this study will provide the respective communities with significant insight into how to prepare high-quality and phase-segregated crystalline epilayers, so that Bi in the required phase can be readily incorporated into the respective device platforms in a scalable manner.

2. Growth Optimization and Characterization of Bi_{TRIG}

Single-elemental thin films entail an immensely diverse temperature range to crystalize in certain phases. Some elements demand ultra-low temperatures (below 0 °C) to crystallize, such as Al and Sn [35,36], while others require temperatures as high as 1400 °C, such as Ta. Bi, however, tends to crystallize at room temperature. In order to grow smooth and high-crystal-quality films of Bi via MBE, the optimum growth parameters, i.e., the growth temperature (T_{sub}) and the thin-film growth rate (R_{TF}), must be identified.

Initially, to acquire the Bi_{TRIG} (001) phase, the growth of Bi films is conducted over a T_{sub} range from -20 °C to 80 °C, where the temperature of the Bi effusion cell is adjusted to maintain $R_{TF} = 10$ nm/h. The morphology of the films is analyzed via scanning electron microscopy (SEM), while the structural characterizations are performed via XRD. The X-ray reflectometry (XRR) scans have provided the necessary information about the thickness and roughness of each film. It is observed that films prepared at low temperatures exhibit smoother surfaces, with roughness increasing significantly with increasing T_{sub}, as can be seen in Figure 2a. Preliminary XRD investigations have revealed diverse structural behavior of the Bi films, including amorphous, single-, and polycrystalline states over the entire range of T_{sub}. The results of qualitative investigations of Bi_{TRIG} (001) crystals, acquired via rocking-curve (RC) analysis of the Bi_{TRIG} (0003) peak, can be visualized in Figure 2a. A similar set of growths is conducted with an increased $R_{TF} = 15$ nm/h, and

while a similar trend is observed, there appears to be a slight improvement in surface and crystal quality. The summarized results of this R_{TF} can be visualized in Figure 2b.
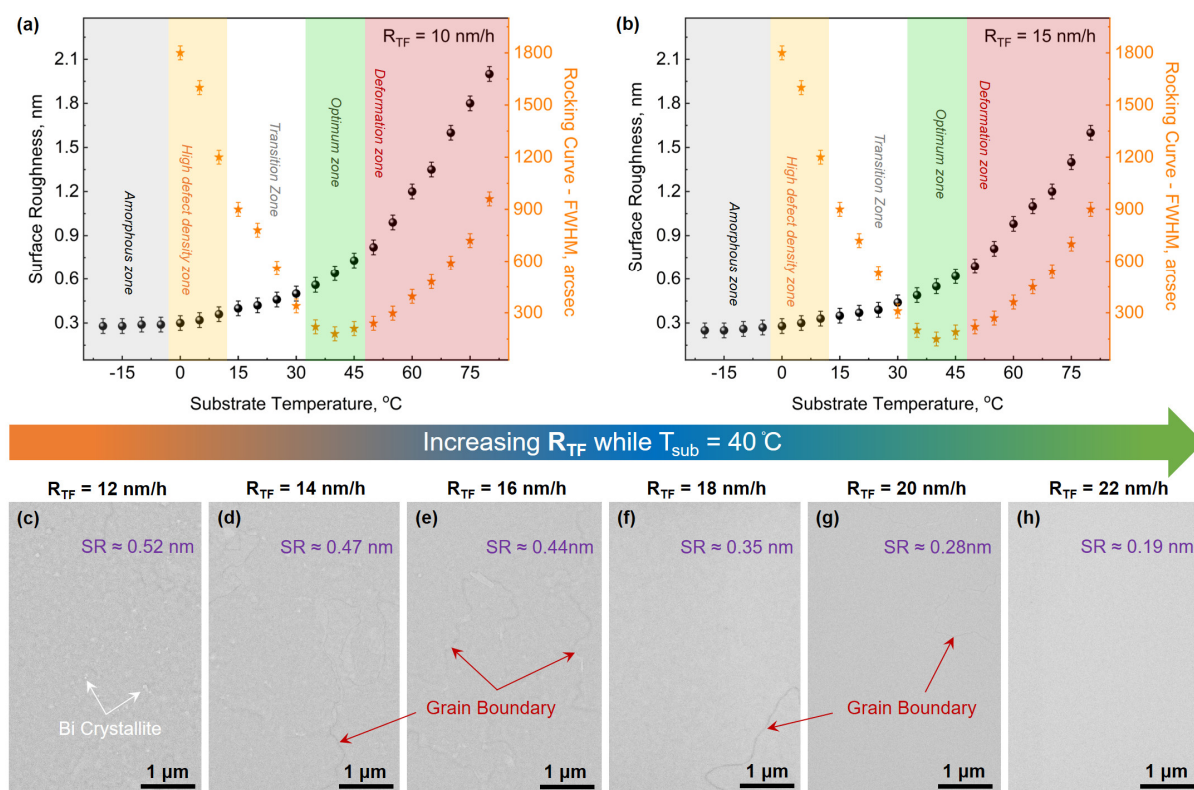

Figure 2. Identification of optimum growth parameters of the Bi_{TRIG} (001) phase. Temperature-dependent changes in surface and crystal quality of Bi_{TRIG} (001) epilayers from $-20\ °C$ to $80\ °C$ prepared with (**a**) RTF = 10 nm/h, (**b**) RTF = 15 nm/h. SEM images of BiTRIG (001) epilayers prepared at Tsub = 40 °C, while RTF is varied from (**c**) 12 nm/h, (**d**) 14 nm/h, (**e**) 16 nm/h, (**f**) 18 nm/h, (**g**) 20 nm/h and (**h**) 22 nm/h, confirming the improved surface quality. SR stands for "surface roughness".

Based on RC analysis, the investigated temperature range is divided into distinct categories that are named "amorphous", "high defect density", "transition", "optimum" and "deformation" zones. The corresponding temperature zones are highlighted in grey, orange, white, green and red, respectively, in Figure 2a,b. The Bi films prepared between $-20\ °C$ and $0\ °C$ are observed to be either amorphous or partially crystalline and are thus placed in the "amorphous zone". The films prepared between $0\ °C$ and $15\ °C$ are witnessed to be crystalline in the Bi_{TRIG} (001) phase; however, these films exhibit a poor crystal quality with RC full-width-half-maxima (FWHM) values above $900''$. This temperature range is thus categorized as the "high defect-density zone". The average grain size and henceforth, the crystal quality is observed to improve continuously throughout the "transition zone" between $15\ °C$ and $35\ °C$, with the RC values reaching close to $300''$. The films prepared in the "optimum zone" with T_{sub} ranging between $35\ °C$ and $50\ °C$ are observed to have the best crystal quality where RC values below $200''$ are achieved. Above $50\ °C$, epilayers are observed to degrade in structural quality, as seen by the increase in RC, and the crystal is observed to transform into a polycrystalline state. This occurs due to an increased density of point and structural defects. This increase in defect density arises as the epilayer becomes more and more thermally unstable with increasing T_{sub}. This temperature range is thus categorized as the "deformation zone". With the identification of the "optimum zone", $T_{sub} = 40\ °C$ is witnessed to deliver the best results and, therefore, is selected for all future growths of the Bi_{TRIG} (001) phase. The focus is then shifted to the identification of optimum R_{TF}. As witnessed in Figure 2a,b, compared to $R_{TF} = 10$ nm/h, both features, i.e., the surface

and crystal quality, are observed to improve at R_{TF} = 15 nm/h. It points toward a higher probability of achieving optimum growths at R_{TF} > 15 nm/h. Following that, several Bi_{TRIG} (001) epilayers are prepared where R_{TF} is gradually (in steps of 2 nm/h) increased from 10 nm/h to 30 nm/h, while T_{sub} is kept constant at 40 °C. The corresponding changes in the surface morphology can be observed via SEM images. A few images, corresponding to key R_{TF} values, are depicted in Figure 2c–h. Through the SEM images, a substantial improvement in the surface quality of the epilayers is observed with increasing R_{TF}. Not only do the Bi crystallites seen at lower R_{TF} vanish, but the averaged grain size is also observed to enlarge significantly. Though epilayers are prepared with R_{TF} up to 30 nm/h, the best results are obtained at R_{TF} = 22 nm/h, and thus, this is selected as the optimum R_{TF}.

With the optimal growth parameters (T_{sub}, R_{TF}) = (40 °C, 22 nm/h) for the Bi_{TRIG} (001) phase found, several epilayers with various thicknesses are prepared to confirm the growth reproducibility by analyzing the surface roughness and crystal quality of each epilayer. After confirming reproducible growths, detailed structural characterizations are performed via XRD, and the lattice parameters of Bi_{TRIG} epilayers are evaluated. Figure 3a represents the measured XRR and simulated curves of a 16 nm thick epilayer. The fitting parameters confirm the ultra-smooth surface, where the measured roughness is even better than the Si (111) substrate itself, which is not something one would expect in MBE. The reason for achieving such an ultra-smooth epilayer resides purely in the structural arrangement of Bi_{TRIG}. As introduced in Figure 1, the Bi_{TRIG} (001) crystals are arranged in vertically stacked bilayers where the height of a single bilayer (3.9 Å) matches almost perfectly with the Si step-edge height (3.87 Å) [5,6]. It is known that Si step edges act as nucleation sites in an early stage of growth [37]. However, during the growth of layered materials such as Bi_2Te_3 and Sb_2Te_3, these step heights lead to the formation of extended structural defects, including antiphase domains and screw dislocations [5,6], whereas, in the case of Bi_{TRIG}, a bilayer with matching height inserts itself at the step edge, neutralizes the formation of extended defects, and results in an improved crystal and surface quality of the epilayer. Figure 3b represents an XRD $\theta/2\theta$ scan confirming the single crystalline behavior of the Bi_{TRIG} (001) epilayer. It is also due to the acquired ultra-smooth surface that the thickness oscillations are observed to appear all the way up to 60° in the diffraction pattern.

Ensuring the single crystallinity of the epilayer, the qualitative investigations are performed via RC ($\Delta\omega$) analysis at the Bi_{TRIG} (0003) peak. Figure 3c depicts the measured RC and the corresponding Gaussian fit, providing the FWHM value of 53 ± 10″. To the best of our knowledge, such a low FWHM value in the MBE-grown Bi-based materials has never been reported. Finally, the lattice parameters are evaluated using the symmetric and asymmetric reciprocal space maps (RSMs). Figure 3d represents a symmetric map across the Bi_{TRIG} (0003) peak. The measured value provided $Q_Z = 2\pi$ (2.529) ± 0.002 nm^{-1} = 1.588 ± 0.002 Å^{-1} which results in an out-of-plane lattice "c" = 11.86 ± 0.01 Å. This acquired value matches perfectly with the reported value in the literature, as mentioned in Figure 1a. It is worth mentioning here that the acquired Q_X value is zero, and thus, any information about the in-plane lattice cannot be extracted. In symmetric setting, x-rays probe only the vertical lattice and provide high-precision information only about the out-of-plane parameter. It, however, lacks any information about the in-plane structure. Depending on material composition and crystal symmetry, XRD peaks differ in their intensity. Considering the Bi_{TRIG} (001) phase, the asymmetric ($1\bar{1}08$) peak is selected to probe the in-plane structure, and the lattice information is extracted. The corresponding RSM is depicted in Figure 3e. As both in-plane lattices are identical (trigonal structure), a single asymmetric peak is sufficient to evaluate the lattice information.
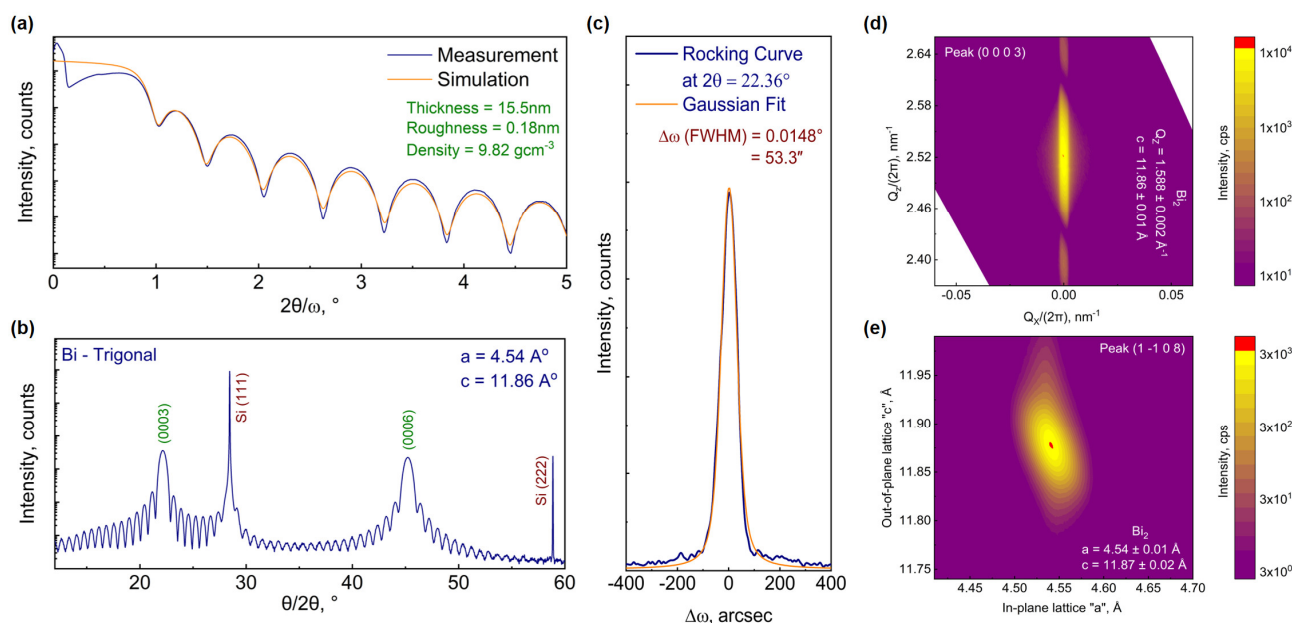
(a)

(b)

(c)

(d)

(e)

Figure 3. XRD characterization of Bi_{TRIG} (001) epilayer prepared at the optimal growth parameters. (**a**) Measured and simulated XRR curves providing information about the thickness and roughness of the epilayer, (**b**) XRD $\theta/2\theta$ scan confirming the single crystallinity, (**c**) rocking curve acquired at Bi_{TRIG} (0003) peak, (**d**) symmetric RSM across Bi_{TRIG} (0003) peak to evaluate the out-of-plane lattice parameter and to identify the presence of any tilted grains and (**e**) asymmetric RSM across Bi_{TRIG} ($1\bar{1}08$) peak to evaluate the in-plane lattice parameters.

3. Structural Transformation and Phase Map

With the successful growth of Bi_{TRIG} (001) epilayers, the focus is shifted to the earlier introduced "deformation zone". As stated in Figure 2, the crystal is observed to exhibit a polycrystalline state when exposed to $T_{sub} > 50\ ^\circ C$. Preliminary XRD investigations indicated that it is either the Bi_{TRIG} (012) or the Bi_{ORTH} phase (as both phases exhibit identical out-of-plane lattices), co-existing with the Bi_{TRIG} (001). The existence of Bi_{ORTH} phase has already been reported in the literature, however, only in the form of non-coalescent ultra-thin (<2 nm) crystallites [21,38,39]. A recent study has reported the presence of 60-nm-wide Bi_{ORTH} crystal grains reaching the thickness of approx. 25 nm in polycrystalline films [26]. Thus, the possibility of growing thick Bi_{ORTH} crystallites is addressed, while the uncertainty of achieving phase-pure, fully coalesced, and high-crystal-quality Bi_{ORTH} epilayers still remains. These obscurities must be tackled before the incorporation of Bi_{ORTH} in nano-devices becomes a reality.

Considering the significance of Bi_{ORTH} to neuromorphic, ferroelectric, and topological communities, a systematic search for the Bi_{ORTH} phase is initiated. Keeping R_{TF} at the optimum value of 22 nm/h, adopted for the Bi_{TRIG} (001) phase, a series of growths are conducted where T_{sub} is gradually (in steps of 2 °C) increased from 40 °C to 120 °C. The structural investigations are performed, and a summary of the acquired results is plotted in Figure 4a. Figure 4b represents the diffraction pattern at select key data points, and Figure 4c–h depict the corresponding morphological alterations via SEM images. At low temperatures, the surface roughness is observed to increase gradually until T_{sub} reaches 70 °C, after which a rapid increment in the surface roughness is evident. This behavior can also be witnessed in Figure 4b with the vanishing thickness oscillations in the corresponding diffraction patterns. The crystal quality of the Bi_{TRIG} (001) phase is observed to continually degrade with increasing T_{sub}, as can be seen with the increasing FWHM values in Figure 4a. After $T_{sub} = 55\ ^\circ C$, the Bi_{ORTH} phase started to emerge, initially with a poor crystal quality that continually improved with increasing T_{sub} until 105 °C. For better understanding, the earlier designated "deformation zone" in Figure 2 is dissected into further sub-groups. In

the region from T_{sub} = 55 °C to 95 °C, only polycrystalline layers (containing both the Bi_{TRIG} (001) and the Bi_{ORTH} phases) are achieved. Due to the continually decreasing fraction of Bi_{TRIG} (001) and increasing ratio of Bi_{ORTH}, this region is named the "transformation zone". Above the transformation zone, a small set of temperatures, i.e., 95–105 °C, have provided the pure phase of the Bi_{ORTH} crystals. Though the surface quality of acquired Bi_{ORTH} is far from optimal, the crystal quality is at an acceptable level, with the FWHM value of the Bi_{ORTH} (020) peak reaching below 300″. This region is designated the "optimum zone (orthorhombic)". Above this temperature, the crystal is only observed to degrade, thus starting the actual "deformation zone".
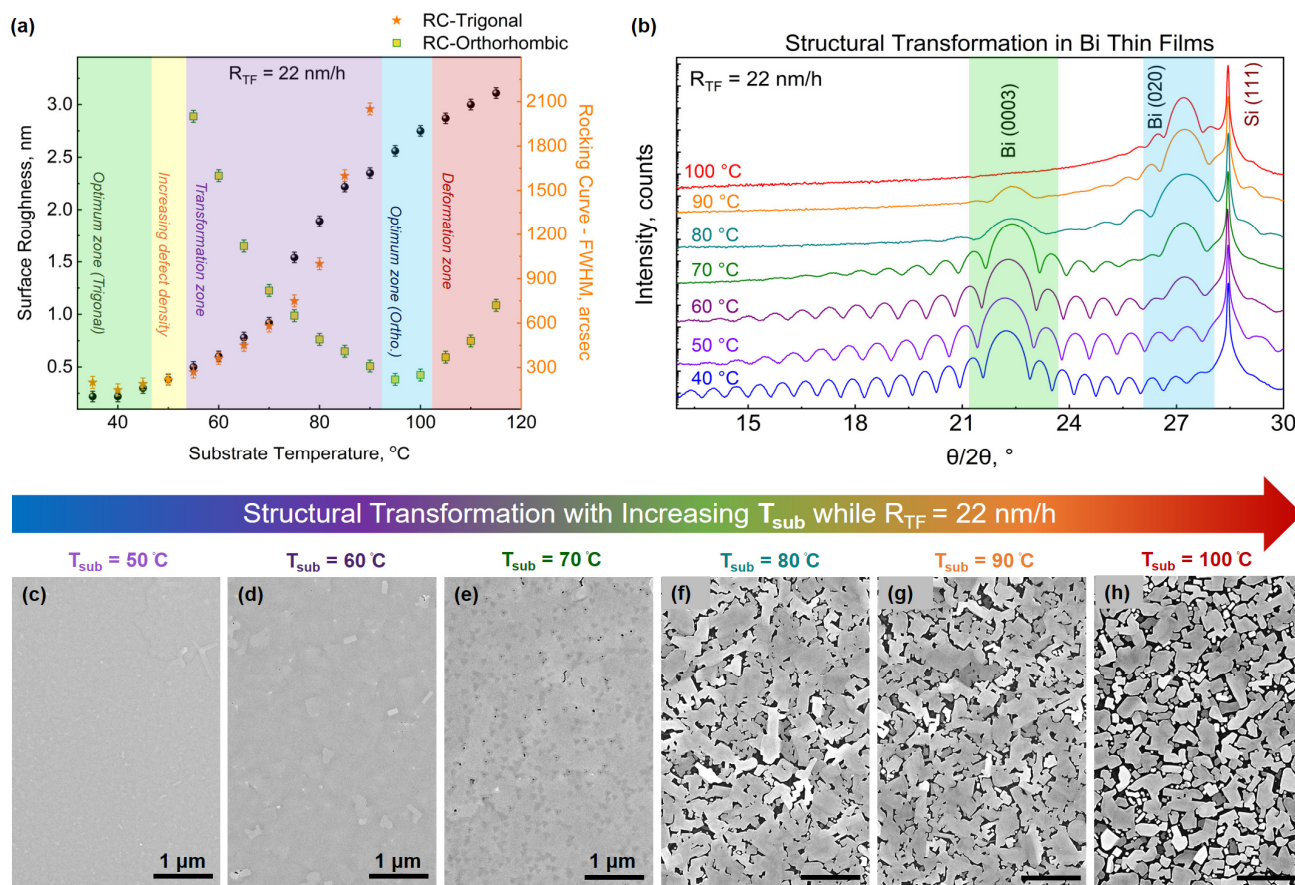

Figure 4. Structural transformation in Bi epilayers. (**a**) Temperature-dependent changes in surface roughness (indicated by black data points) and crystal quality of Bi epilayers from 40 °C to 120 °C, prepared with R_{TF} = 22 nm/h, result in continually changing structures from Bi_{TRIG} (001) to Bi_{ORTH} (010) phase passing through polycrystalline states. (**b**) The corresponding diffraction pattern at the select key temperatures indicating the continually reducing and enhancing contributions from Bi_{TRIG} (001) and Bi_{ORTH} (010) phases, respectively. For better understanding, Bi_{TRIG} (0003) and Bi_{ORTH} (020) peak regions are highlighted with green and blue, respectively. The corresponding changes in surface morphology via SEM images when the epilayer is prepared at (**c**) T_{sub} = 50 °C, (**d**) 60 °C, (**e**) 70 °C, (**f**) 80 °C, (**g**) 90 °C, and (**h**) 100 °C.

Before the focus is shifted to optimizing the surface quality of Bi_{ORTH} crystals, a couple of points are worth mentioning here. (1) For the first time, phase-pure growth of Bi_{ORTH} crystals having a thickness ≫ 2 nm is successfully achieved via MBE. (2) Though Bi_{ORTH} peaks started to emerge at T_{sub} > 55 °C, a sudden change in crystal morphology and structural alignment is observed to transpire in the transformation zone between 70 °C and 80 °C. Referring to Figure 4e,f, the presence of a relatively smooth and almost fully coalesced layer at 70 °C is suddenly converted into rough and randomly ordered

crystals at 80 °C, confirming a sudden rather than a gradual change in the crystal structure. Moreover, notice the change in XRD pattern between 70 °C and 80 °C in Figure 4b, where a clear indication of contributing layer thickness change can be perceived. The preliminary characterizations of the in-plane structure indicate that from 55 °C to 70 °C, the peak appearing at $2\theta = 27.2°$ belongs to the Bi_{TRIG} (012) phase, and not the Bi_{ORTH}. Above 70 °C, however, the crystal re-arranges itself, undergoes a few transformations, and converts into the Bi_{ORTH} phase that slightly differs from the Bi_{TRIG} (012) orientation. It is interesting to note that the out-of-plane lattices in Bi_{TRIG} (012) and Bi_{ORTH} match perfectly, and this is the reason that no significant shift in the diffraction peak is observed. At this stage, it can be assumed that the Bi_{TRIG} (012) orientation acts as an intermediate stage between Bi_{TRIG} (001) and Bi_{ORTH} phases. Further discussions on similarities and differences between both phases, i.e., the Bi_{TRIG} (012) and the Bi_{ORTH}, will be conducted at a later stage; however, right now the focus will be kept on the surface optimization of the Bi_{ORTH} phase.

Based on the analysis of Figure 4, it is clear that the Bi_{ORTH} phase can only be segregated at high temperatures (around 100 °C). What role R_{TF} plays in the phase segregation of Bi films is still unknown. Furthermore, it is also important to study the impact of R_{TF} on surface quality to achieve smooth and fully coalesced Bi_{ORTH} epilayers if possible. To answer these questions, a detailed and systematic growth study of Bi films is conducted where T_{sub} is altered in steps of ± 2 °C between the two identified "optimum zones" depicted in Figure 4a. R_{TF} is also adjusted in steps of 2 nm/h, starting from 6 nm/h to 30 nm/h. All of the prepared films are investigated via XRD, and the information about crystal phase, crystal quality, and surface roughness is evaluated and depicted with the help of colored maps in Figure 5.

The impact of growth parameters (T_{sub}, R_{TF}) on the crystal phase can be visualized in Figure 5a. To identify the presence of a single phase in the epilayer is straightforward; however, the question arises as to how to distinguish the relative presence of a specific phase in the polycrystalline films. To understand the impact of changing growth parameters, phase-specific diffraction peaks, i.e., Bi_{TRIG} (0003) and Bi_{ORTH} (020), are selected. The measured peak intensities in the diffraction pattern, belonging to a specific film thickness, are multiplied with the corresponding theoretically predicted intensities. The ratio $R_{(0003)}/R_{(020)}$ is evaluated and utilized to identify the relative presence of a certain phase in the epilayer. Similarly, the corresponding information at each data point about the surface roughness and crystal quality, RC-FWHM, for Bi_{TRIG} (0003) and Bi_{ORTH} (020) peaks is represented in Figure 5b–d, respectively.

It can be clearly observed that low T_{sub} and high R_{TF} facilitate the achievement of the Bi_{TRIG} (001) phase. Conversely, at high T_{sub} and low R_{TF}, films crystallize only in the Bi_{ORTH} phase. However, none of the above-mentioned parameters are optimal. For Bi_{TRIG} (001), high R_{TF} results in smoother films, as can be witnessed in Figure 5b; however, after a certain point, the crystal quality starts to degrade with increasing density of rotational domains and reduced grain size, resulting in enhanced RC-FWHM values that can be visualized in Figure 5c. The best crystal quality is achieved at R_{TF} between 22 and 26 nm/h. The optimum growth zone for Bi_{TRIG} (001) is highlighted with the white-dotted box in Figure 5b,c. As far as the Bi_{ORTH} phase is concerned, films achieved at low R_{TF} values exhibit enormously high surface roughness due to the formation of non-coalescing crystallites. Such films are not suitable for integration into any electronic device. With increasing R_{TF}, the surface roughness is witnessed to improve significantly; however, the temperature requirements to keep the Bi_{ORTH} phase segregated increase as well. Epilayers with the best crystal quality and improved surfaces of the Bi_{ORTH} phase are achieved at high T_{sub} and R_{TF} values, a region marked with the green-dotted box in Figure 5b,d.
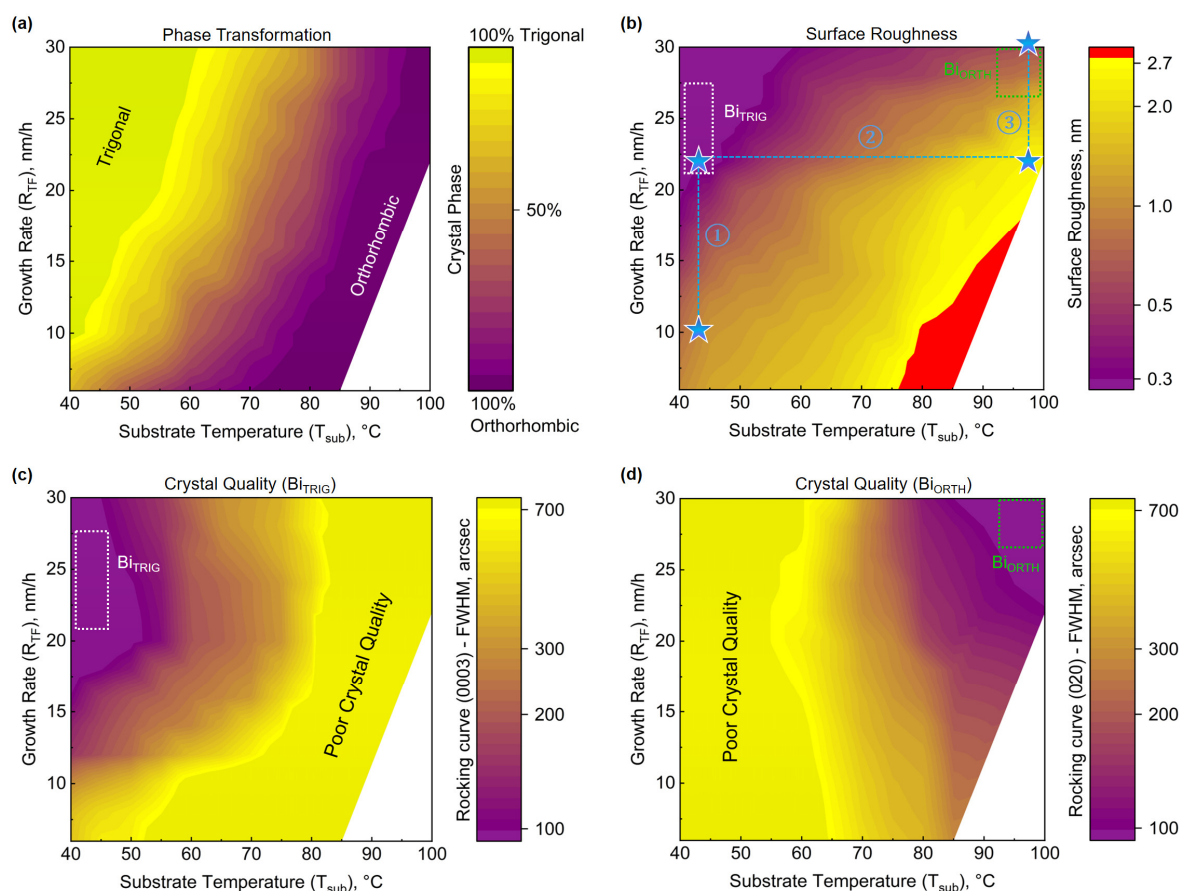
Figure 5. Growth parameter-dependent structural transformation map. A summary of 445 data points where the growths are performed between the two distinct optimum zones, i.e., trigonal and orthorhombic phases. XRD evaluations are abridged in colored maps providing the information about (**a**) the relative presence of certain allotropes between the Bi_{TRIG} (001) and the Bi_{ORTH} (010) phases in the epilayers, (**b**) the surface roughness of the epilayers at the corresponding data points. The red color in the map indicates the rms roughness exceeds 3 nm. The path adopted during initial investigations of the structural optimization and the phase transformation in Bi thin-films is highlighted with blue dotted lines, where, the stars represent key data points. The sub-paths ① and ③ represent R_{TF} dependent surface optimization of the Bi_{TRIG} (001) and the Bi_{ORTH} (010), respectively while ② represents the temperature dependent phase transformation in Bi thin films with R_{TF} is kept at 22 nm/h. The qualitative figure of merit for the structural quality of the trigonal and the orthorhombic phases, at the corresponding data points on the map, are depicted in (**c**) and (**d**) by measuring the rocking curves at Bi_{TRIG} (0003) and Bi_{ORTH} (020) peaks, respectively.

Observing the phase transformation map, it is evident that almost 80% of the data points resulted in the formation of polycrystalline films. It emphasizes the importance of identifying phase-specific optimum growth zones. Moreover, the achievement of pure-phase and thick crystalline films of the Bi_{ORTH} phase has not been reported to date. Thus, the transformation maps depicted in Figure 5 not only helped in achieving phase-pure epilayers of Bi_{ORTH} systematically, but also provided a platform that serves as a reference for all future requirements of phase-segregated growths of Bi nanofilm allotropes. To highlight the importance of these maps, the path of parameter selection in this study is retraced in Figure 5b, which leads to the next step, i.e., the surface optimization of Bi_{ORTH} films.

4. Growth Optimization of Bi_{ORTH}

As depicted in Figure 5b, with an increment in R_{TF}, the surface roughness of Bi_{ORTH} epilayers improves considerably. By further increasing R_{TF} to 32 nm/h, almost fully

coalesced films are successfully achieved. Though random small holes are still observed in the films, a majority of the surface is observed to be fully coalesced. The corresponding changes in morphology can be visualized with the help of SEM images in Figure 6a–f.
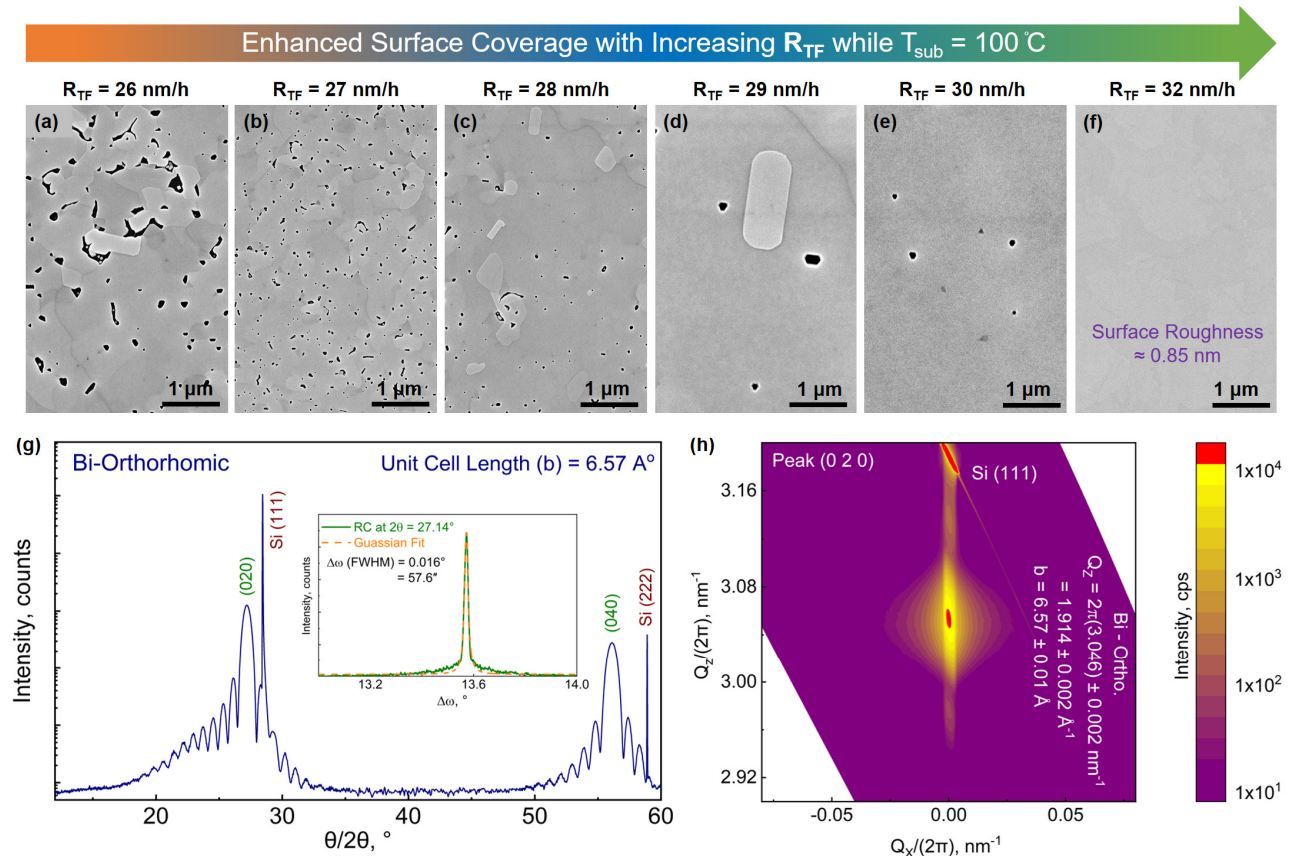

Figure 6. Growth optimization and structural characterization of Bi_{ORTH} epilayers. SEM images represent continually improving surface coverage when the epilayers are prepared with (**a**) R_{TF} = 26 nm/h, (**b**) 27 nm/h, (**c**) 28 nm/h, (**d**) 29 nm/h, (**e**) 30 nm/h and (**f**) 32 nm/h while T_{sub} is kept at 100 °C. (**g**) Diffraction pattern of Bi_{ORTH} epilayer prepared at 32 nm/h, (inset) rocking curve acquired at Bi_{ORTH} (020) peak, (**h**) symmetric RSM acquired at Bi_{ORTH} (020) peak, providing information about the out-of-plane lattice parameters and confirming high crystal quality of the Bi_{ORTH} epilayer.

Later, XRD-based structural characterizations are performed, and the diffraction pattern of the best acquired film at R_{TF} = 32 nm/h is plotted in Figure 6g. The appearance of the thickness oscillations in Figure 6g, compared to one depicted in Figure 4b at T_{sub} = 100 °C and R_{TF} = 22 nm/h, is an indication of significant improvement in the surface quality. The RC measurement at the Bi_{ORTH} (020) peak, depicted as inset in Figure 6g, has provided the FWHM value of $58 \pm 10''$, which is comparable to the crystal quality of the Bi_{TRIG} (001), depicted in Figure 3c. To evaluate the out-of-plane lattice parameters and to identify the presence of any tilted grains, a symmetric RSM across the Bi_{ORTH} (020) peak is acquired and depicted in Figure 6h. The measured value provided $Q_Z = 2\pi \times (3.046) \pm 0.002$ nm^{-1} = 1.914 ± 0.002 Å^{-1}, which results in an out-of-plane lattice "b" = 6.57 $\pm$ 0.01 Å. The acquired value is in good agreement with earlier reported results on Si (111) substrates [21,26,27]. The symmetric RSM also confirms the absence of any tilted or heavily misaligned grains, pointing to a high-quality epilayer. As discussed earlier, to extract the in-plane lattice parameters, asymmetric diffraction data must be attained. However, before any asymmetric measurements can be performed, it is important to gain a better understanding of how the domains prefer to align with respect to the substrate.

5. Domain Alignment of Bi Nanofilm Allotropes

To comprehend the in-plane alignment of domains with respect to the substrate, the rotational symmetry of lattices via conventional φ-scanning is investigated. Figure 7 represents detailed information on domain alignment in various Bi phases. A trigonal lattice exhibits 3-fold rotational symmetry. While growing a trigonal crystal on a hexagonal surface, e.g., Si (111), the crystal may exhibit 60° in-plane rotated domains. A similar scenario is observed in Bi_{TRIG} (001) epilayers, as depicted in Figure 7a. The figure on top is a 3D pole-figure map, acquired via probing the Bi_{TRIG} $(1\bar{1}02)$ peak to identify all present domains in the epilayer, as this peak exhibits the highest diffraction intensity. It is evident that the epilayer contains twin domains, i.e., 60° rotated domains that can also be visualized with the help of an illustration containing two 60° rotated colored triangles placed inside the pole-figure map. Moreover, the domains are observed to be collinear with the substrate peak, referring to the 60°, 180°, and 300° marks in the map. At the bottom of Figure 7a, a 2D cut at $\chi = 55.7°$ is plotted. From the intensity, it is evident that both rotational domains have not populated the epilayer equally; rather, a 1:5 ratio is observed. Other trigonal crystals, e.g., Bi_2Te_3 and Sb_2Te_3, are also reported to exhibit a similar trend when grown on Si (111) [5,6]. However, in the case of Bi_{TRIG} (001), a minor difference is perceived. It is observed that the Bi_{TRIG} (001) exhibits a preferential alignment to Si (220), which is a behavior opposite to that of Bi_2Te_3 and Sb_2Te_3 crystals that favor Si (311) instead. Why Bi_{TRIG} behaves differently from other family compounds is not clear at this point and requires further insight with the support of theoretical modeling. Nevertheless, a similar trend is observed in all Bi_{TRIG} (001) epilayers prepared at T_{sub} from 5 °C to 50 °C, while $R_{TF} > 10$ nm/h.

During this investigation, it was discovered that for $T_{sub} > 50$ °C, the crystal enters the "transformation zone" where unique in-plane transitions are observed, as visualized in Figure 7b. The 60° rotated domains of Bi_{TRIG} (001) are highlighted with green-colored regions. Starting from $T_{sub} = 54$ °C, distinctive three-pointed peaks start to emerge in between Bi_{TRIG} (001) domains. These domains, similar to the Bi_{TRIG} (001), are observed to exhibit 60° periodicity; however, their alignment in between the Bi_{TRIG} peaks placed them at a 30° offset with the substrate collinearity. These domains are highlighted with purple-colored regions in Figure 7b. Alongside the appearance of exotic three-pointed peaks in the φ-scan, a diffraction peak at $2\theta = 27.2°$ is witnessed to emerge, as discussed in Figure 4b, which confirms that these two events are linked. Moreover, as the exotic peaks in the φ-scan exhibit 60° periodicity, they cannot originate from the Bi_{ORTH} phase and must be connected to the Bi_{TRIG} (012) orientation, as the Bi_{TRIG} (012) also exhibits the facilitating diffraction peak at $2\theta = 27.2°$. This assumption, however, requires further investigation. With increasing T_{sub}, the relative intensity of these uniquely oriented peaks is also observed to rise until $T_{sub} = 70$ °C.

Above 70 °C, another in-plane transition is witnessed where each three-pointed exotic peak is observed to split into two distinct peaks that are 30° apart from each other and $\pm 15°$ shifted from the position of their origin, highlighted by the black-dotted arrows in Figure 7b. Thus, the newly originated peaks exhibit a 45° offset from the substrate collinearity. This transition gives rise to 12 peaks that exhibit 30° periodicity, along with six peaks originating from the Bi_{TRIG} (001), as observed in an epilayer prepared with $T_{sub} = 75$ °C and depicted in Figure 7b. As far as the diffraction pattern is concerned, no significant change in peak positions is observed. The morphology of the crystal, on the other hand, is observed to transform completely, as discussed in Figure 4. As the appearance of 12 distinct peaks with 30° periodicity is a hallmark of cubic-like structures when aligned on a hexagonal surface [40], this second stage of transition can be linked to the rise of the Bi_{ORTH} phase.
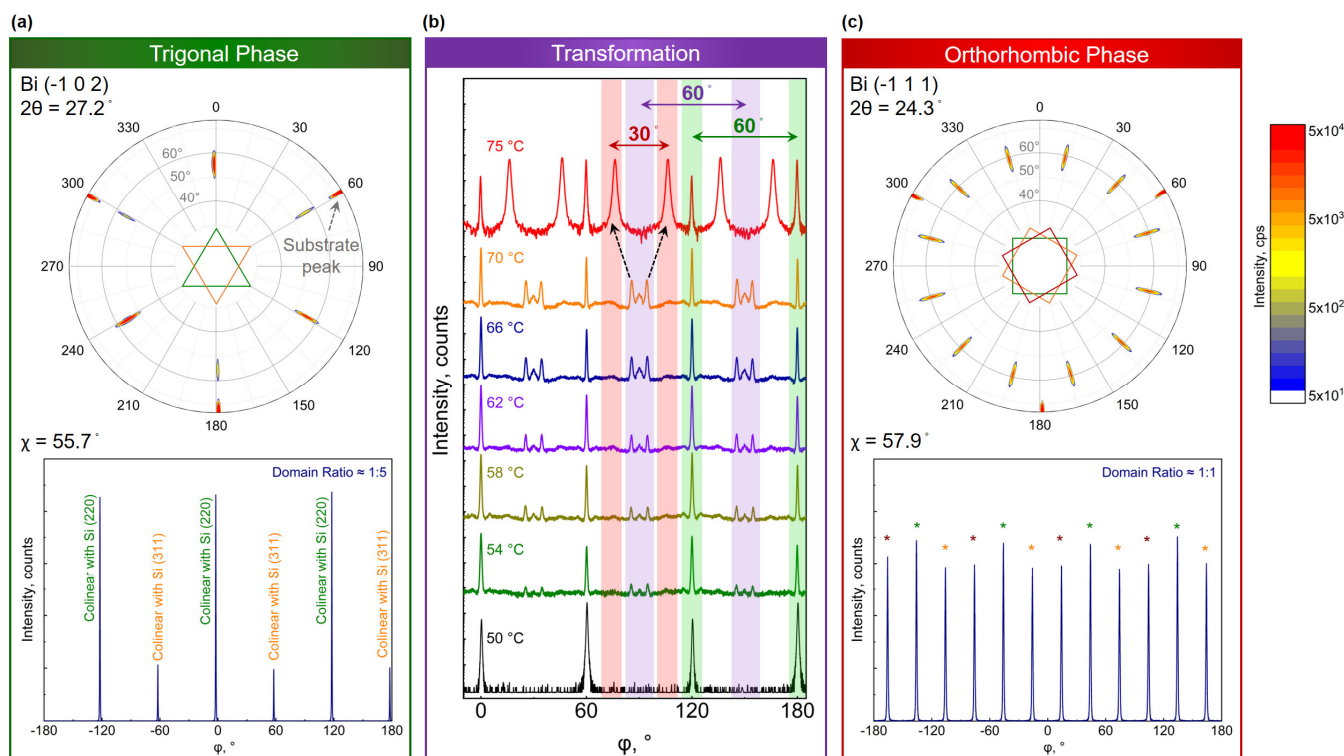
Figure 7. Domain analysis of Bi nanofilm allotropes and their alignment with respect to the substrate. (**a**) Analysis of the $Bi_{TRIG}(001)$ epilayers performed by probing the $(1\bar{1}02)$ peak. (**Top**) A pole-figure map representing six distinct peaks originating from two 60° in-plane rotated trigonal domains. (**Bottom**) The φ-scan, a 2D cut at χ = 55.7°. (**b**) A series of φ-scans representing temperature-dependent structural transformation in Bi epilayers. The emergence of three-pointed distinct peaks is found to be related to the $Bi_{TRIG}(012)$, whereas the transformation of those three-pointed peaks into 12 distinct peaks is an indication of the orthorhombic crystal structure. (**c**) Analysis of the Bi_{ORTH} (010) epilayers conducted via probing $(\bar{1}11)$ peak. (**Top**) A pole-figure map representing 12 distinct peaks originating from three 30° in-plane rotated orthorhombic domains highlighted with district colored and rotated squares. (**Bottom**) The φ-scan, a 2D cut at χ = 59.9°, provides information about the relative presence of domains in the epilayer. Each peak is marked with a color that corresponds to the associated domain.

With further increase in T_{sub}, peaks associated with the Bi_{TRIG} (001) are witnessed to diminish, while 30° periodic Bi_{ORTH} peaks are observed to improve in intensity until T_{sub} reaches 95 °C. Above 95 °C, epilayers are observed to crystallize in the Bi_{ORTH} phase only. Figure 7c depicts a 3D pole-figure map of the Bi_{ORTH} epilayer acquired via probing $(\bar{1}11)$ peak and a 2D cut at χ = 57.9°, confirming the presence of only 12 in-plane peaks. As the orthorhombic lattice exhibits four-fold rotational symmetry, the alignment of domains in the epilayer is illustrated with the help of three distinct colored boxes rotated by 30° and placed inside the pole-figure map. The four-fold rotational symmetry can also be witnessed in a 2D φ-scan where each peak is color-identified with the associated domain. During the first and second in-plane transitions in Figure 7b at 54 °C and 75 °C, respectively, the non-collinearity of the crystal peak with respect to the substrate was explained. Here, all three Bi_{ORTH} domains can be visualized to exhibit a 15°, 45°, and 75° offset with respect to the substrate peak, respectively.

Through detailed analyses of φ-scans, it can be summarized that from the "optimum zone (trigonal)", i.e., (T_{sub}, R_{TF}) = (40 °C, 22 nm/h), to the "optimum zone (orthorhombic)", i.e., (T_{sub}, R_{TF}) = (100 °C, 32 nm/h), epilayers go through four major states. (1) All epilayers before entering the "transformation zone" exhibit twin domains with six distinct peaks originating from the Bi_{TRIG} (001) phase. (2) Epilayers prepared at 50 °C < $T_{sub} \leq$ 70 °C

exhibit polycrystalline structures featuring the Bi_{TRIG} (001) along with the Bi_{TRIG} (012) orientation. The exotic three-pointed peaks are found to be related to the Bi_{TRIG} (012) orientation, which is confirmed via asymmetric RSM that can be seen in Supplementary Figure S1. (3) Epilayers prepared at 70 °C < T_{sub} < 95 °C also exhibit polycrystalline structures; however, here, the Bi_{TRIG} (001) and the Bi_{ORTH} (010) phases are realized. As the out-of-plane lattices in the Bi_{ORTH} (010) and the Bi_{TRIG} (012) orientations match with good approximation, no significant change in the diffraction pattern is observed (Figure 4b). The signature 12 peaks of orthorhombic crystal along with six peaks of the Bi_{TRIG} are observed in this region. It is also important to point out here that, for a short temperature range, epilayers are also witnessed to contain all three phases, including Bi_{TRIG} (001), Bi_{TRIG} (012) and Bi_{ORTH} (010). As the temperature range to host these three phases is very narrow, φ-scans are not presented in Figure 7. (4) Finally, the phase-pure Bi_{ORTH} epilayers are acquired at $T_{sub} \geq$ 95 °C, where only 12 distinct peaks of three rotational domains are observed in the epilayer.

6. Evaluation of Lattice Parameters of Bi_{ORTH}

After a thorough understanding of domain alignment in the various Bi phases, the focus is set to evaluate the 2D in-plane lattices of Bi_{ORTH} using asymmetric RSMs. Based on reported Bi_{ORTH} lattices [21,26], the Bi_{ORTH} $(06\bar{2})$ and the Bi_{ORTH} (260) peaks are probed (details can be found in Supplementary Figures S2–S4), and unexpectedly, no diffraction is observed. It indicates the selected lattice parameters are incorrect. After several failures to probe individual in-plane lattices, successful diffractions are finally achieved for 45° rotated the Bi_{ORTH} $(15\bar{1})$ and the Bi_{ORTH} $(\bar{1}71)$ peaks, and, as expected (orthorhombic crystal, unlike cubic, exhibits nonequivalent in-plane lattices), dual diffraction peaks are detected. These peaks contain information about both in-plane lattices but are not ideal for extracting lattice information as they have reduced diffraction intensity. Nonetheless, by probing these peaks, the diffraction is successfully witnessed for each 30° rotated domain, as explained in Figure 7c. One of the asymmetric RSMs acquired at the Bi_{ORTH} $(15\bar{1})$ peak is depicted in Figure 8a, where the in-plane lattice parameters are found to be 4.49 ± 0.02 Å and 4.81 ± 0.02 Å, respectively. The measured lattices are in close agreement with reported values of Bi_{ORTH} on HOPG [10,13,39], but they differ slightly from reported values acquired on Si (111) [21,26,27,29,41].

Analyzing RSM in Figure 8a, it can be seen that both in-plane lattices are unequal, having a difference of Δd = 0.32 Å. Moreover, a minute difference along the z-direction of both peaks is also evident and is measured to be Δh = 0.09 Å, which can be related to buckling [13,15,29]. Buckling is a strain-induced deformation in a crystal and can be described as the height difference between two atoms of the same monolayer [13]. During the lattice transformation of Bi_{TRIG} (012), a phase known to exhibit strong buckling, into Bi_{ORTH}, the strain relaxation in the crystal modifies the buckling height to reduce it. In this work, the measured buckling of 0.09 Å affirms the relaxed state of Bi_{ORTH} in comparison to Bi_{TRIG} (012) [13,15,21]. Almost all studies on Bi_{ORTH} have reported buckling to be present, and the extent of buckling is reported to have a huge influence on the topological properties [10,13,15,21]. According to Lu et al., the measured value of buckling height, i.e., 0.09 Å in this work, places Bi_{ORTH} crystals in a topological regime [13].

Though in-plane lattices are successfully measured, there remains a question of why the diffraction is not observed for conventional high-intensity peaks, i.e., the Bi_{ORTH} $(06\bar{2})$ and the Bi_{ORTH} (260), while a low-intensity peak such as the Bi_{ORTH} $(15\bar{1})$ is probed successfully. The answer resides in the unique structural arrangement of the Bi_{ORTH} crystal on Si (111) substrates. The 45° in-plane rotation of the Bi_{ORTH} lattice, when projected on Si $[1\bar{1}0]$ and Si [211] planes, together with the matching out-of-plane lattice, facilitates the formation of a pseudo-cubic sub-lattice, as depicted in Figure 1g–i. To date, RSM-based structural investigations of the Bi_{ORTH} phase have not been reported, which presented certain challenges in the evaluation of diffraction peaks. Nonetheless, based on the values evaluated by the Pythagorean theorem stated in Equations (1)–(3) and the matching out-of-

plane lattice parameters, Bi in a pseudo-cubic structure (Bi_{CUB}) is estimated to arrange itself with "a" ≈ "b" ≈ "c" ≈ 6.57 Å. Adopting Bi_{CUB} parameters, high-intensity asymmetric peaks are selected, and asymmetric RSMs at the Bi_{CUB} $(\bar{2}40)$ and the Bi_{CUB} $(04\bar{2})$ peaks are successfully acquired, as shown in Figure 8b,c respectively. The difference in the out-of-plane lattices acquired via the Bi_{CUB} $(\bar{2}40)$ and the Bi_{CUB} $(04\bar{2})$ can be linked directly to the Bi_{ORTH} $(15\bar{1})$ in Figure 8a. In other words, the Bi_{ORTH} and the Bi_{CUB} are two different representations of the same crystal structure. To confirm the lattice symmetry, RSMs at the Bi_{CUB} $(\bar{2}40)$ and the Bi_{CUB} $(04\bar{2})$ peaks are also acquired for 30° and 60° rotated domains, and similar results are attained that can be visualized in Supplementary Figures S5 and S6.

$$a_{CUB} = \sqrt{a_{ORTH}^2 + c_{ORTH}^2} \tag{1}$$

$$a_{CUB-8\ nm} = \sqrt{4.49^2 + 4.81^2} \approx 6.58 \tag{2}$$

$$a_{CUB-25\ nm} = \sqrt{4.57^2 + 4.74^2} \approx 6.58 \tag{3}$$
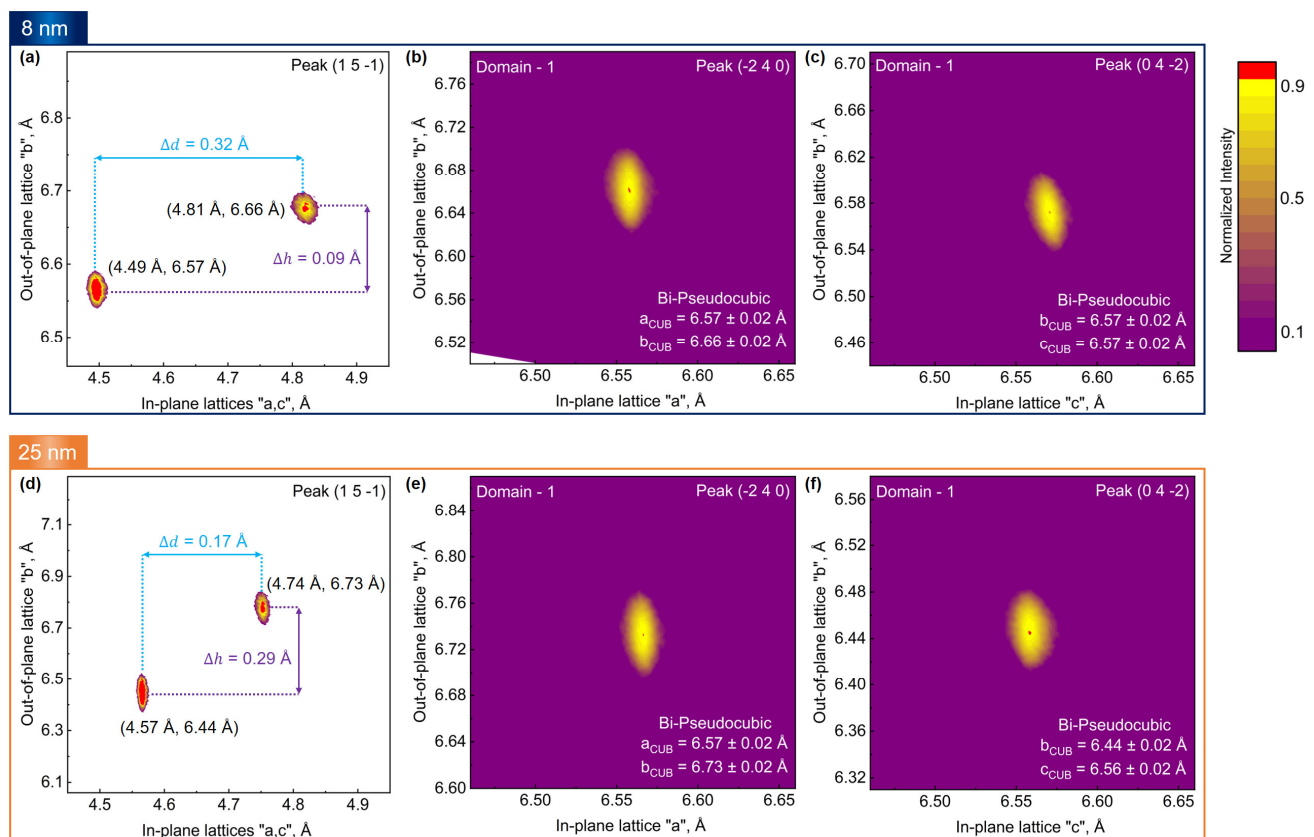
Figure 8. Evaluation of in-plane lattice parameters of the Bi_{ORTH} (010) epilayers via asymmetric RSM. (**a**) A map acquired at the Bi_{ORTH} $(15\bar{1})$ peak in an 8.4 nm thick epilayer, where Δd represents the difference in length between in-plane lattices while Δh represents buckling, i.e., high difference between Bi atoms of the same monolayer; the 45° in-plane rotation led to the formation of pseudo-cubic sub-lattice, and the acquired maps at the Bi_{CUB} $(\bar{2}40)$ and the Bi_{CUB} $(04\bar{2})$ peaks are represented in (**b**,**c**), respectively. Similar measurements are performed in a 25 nm thick epilayer at (**d**) Bi_{ORTH} $(15\bar{1})$, (**e**) Bi_{CUB} $(\bar{2}40)$ and (**f**) Bi_{CUB} $(04\bar{2})$ peaks, where a difference in buckling height in (**d**) is observed to enhance from 0.09 Å to 0.29 Å.

During RSM investigations, it was observed that thickness plays a critical role in the structural arrangement of the Bi_{ORTH} lattice. RSMs acquired at the the Bi_{ORTH} $(15\bar{1})$ peak

in a 25 nm thick epilayer are depicted in Figure 8d, where the in-plane lattice parameters are found to be 4.57 ± 0.02 Å and 4.74 ± 0.02 Å, respectively. It is evident that both in-plane lattices have shifted slightly, and the difference between them (Δd) is reduced from 0.32 Å to 0.17 Å. Moreover, the buckling height is witnessed to enhance three-fold, from 0.09 Å to 0.29 Å, when the layer thickness is increased from 8 nm to 25 nm, indicating the increased strain in the Bi_{ORTH} crystal. A similar effect is also observed by measuring the Bi_{CUB} $(\bar{2}40)$ and the Bi_{CUB} $(04\bar{2})$ peaks depicted in Figure 8e,f, respectively, confirming the enhanced buckling height in the thick Bi_{ORTH} film. An interesting point to mention here is, that, no thickness dependent change in the in-plane lattices of Bi_{CUB} is observed. It is due to the fact that the projected values of both sets of orthorhombic lattices at 8 nm (Figure 8a) and 25 nm (Figure 8d) remain almost identical (Equation (3)). The acquired lattices in a 25 nm-thick Bi_{ORTH} epilayer are found to be in close agreement with earlier reports on Si (111), although the buckling height is still much smaller than the reported value of 0.5 Å [21,26,27,29,41].

7. Atomic-Scale Structural Characterization

Finally, using scanning transmission electron microscopy (STEM), atomic-scale structural characterizations of Bi nanofilm allotropes are performed. Epilayers from three distinct phases, including the Bi_{TRIG} (001), the Bi_{ORTH} (010), and a polycrystalline phase acquired at $T_{sub} = 70\ °C$ containing both the Bi_{TRIG} (001) and the Bi_{TRIG} (012) orientations, are selected. The selected epilayers are then probed via focused ion beam (FIB), and lamellae at the cross-sections of each epilayer along Si $[1\bar{1}0]$ and Si [211], are extracted. The Bi epilayers, unlike other layered materials, presented serious challenges both in extracting lamellae and in acquiring high-resolution STEM images. On several occasions, the lamellae were observed to be amorphous with a heavily deformed interface at the substrate. A few examples are summarized in Supplementary Figures S7–S10. Such a behavior can be explained by a poor thermal stability of Bi. By carefully fabricating lamellae at low energies in FIB and reducing the exposure time under the focused electron beam during STEM, successful structural investigations are performed, and the key results are summarized in Figure 9.

Figure 9a depicts an overview high-angular annular dark-field (HAADF) image of the Bi_{TRIG} (001) epilayer along the Si $[1\bar{1}0]$ projection. An atomically sharp interface between Bi_{TRIG} and Si (111) can be visualized in Figure 9b,c, depicting HAADF and bright-field (BF) images, respectively. Before the periodic stacking of Bi bilayers, the appearance of a Bi monolayer passivating the dangling bonds at the Si (111) surface, is evident. It affirms the formation of 1×1—Bi surface, a 2D sheet of Bi, as a seed layer for epitaxial growth of Bi_{TRIG} (001). A magnified HAADF image of the central region, away from the interface, is depicted in Figure 9d, affirming the high structural quality of the epilayer without the appearance of any extended defects.

During the investigation of polycrystalline epilayers, the presence of the Bi_{TRIG} (012) oriented crystals, predicted during the analysis of domain alignment in Figure 7b, is successfully observed. A HAADF image focusing on the Bi_{TRIG} (012) oriented grain is depicted in Figure 9e, while a low-pass filtered, magnified image of a central region is depicted in Figure 9f. It clearly indicates a black-phosphorus-like puckered structure of Bi atoms; however, unlike the black phosphorus, the Bi_{TRIG} (012) exhibits a strong buckling between the Bi atoms that can also be visualized in the image. Atomic distance measurements via line profiles of the HAADF image have revealed the buckling height to vary between 0.43 ± 0.02 Å and 0.48 ± 0.02 Å in a Bi_{TRIG} (012) monolayer. The difference between various measured values at different positions in the acquired image can be linked to localized changes in the tilt angle as the lamella is witnessed to be heavily bent due to the curtain effect imposed by the deposited Pt layer during FIB. Nevertheless, even the smallest measured value of buckling in the Bi_{TRIG} (012) orientation is almost half an order larger than the XRD-measured value of buckling in Bi_{ORTH} thin films, depicted in Figure 8a.

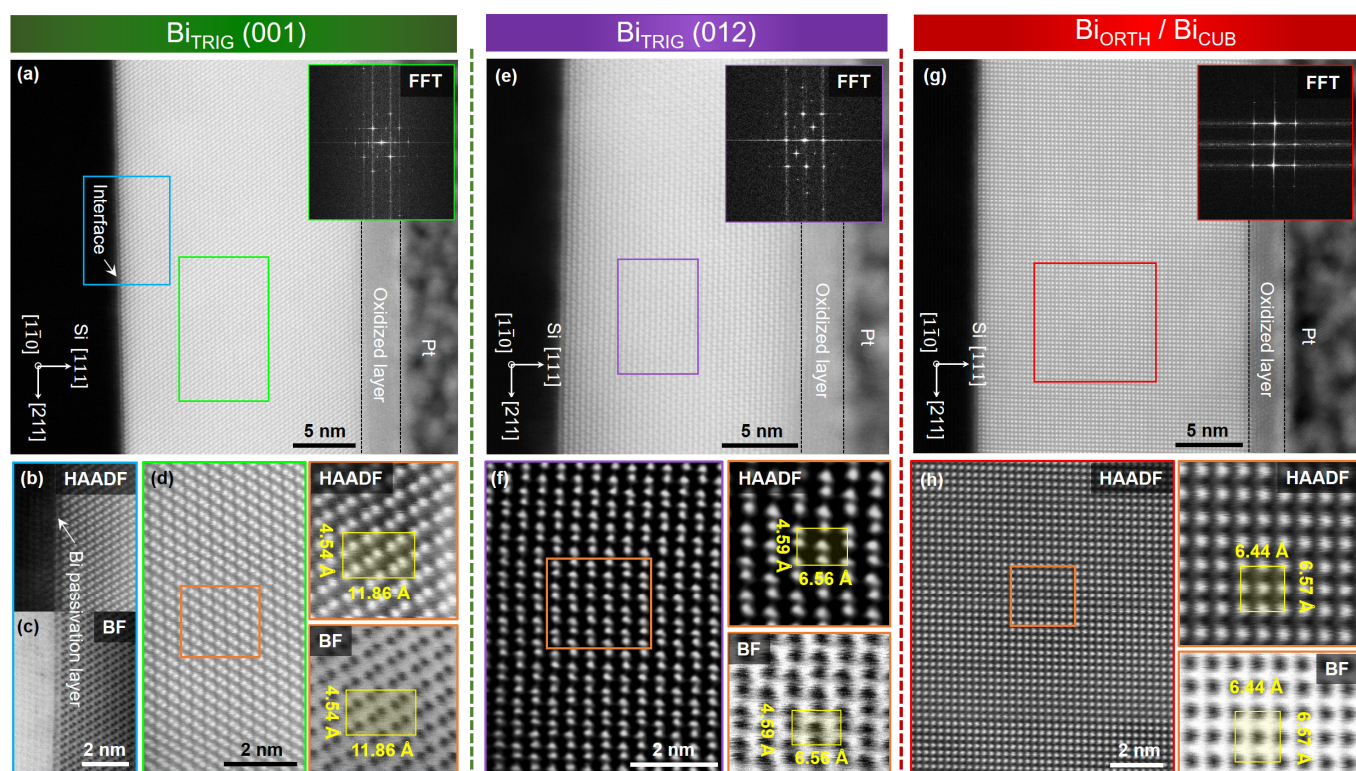**Figure 9.** STEM investigations of Bi nanofilm allotropes. (**a**) A cross-sectional HAADF image of Bi$_{TRIG}$ (001) epilayer acquired along Si $[1\bar{1}0]$ projection. The magnified region at the interface can be visualized via (**b**) HAADF and (**c**) BF images, respectively. The central marked region is further magnified and depicted in (**d**), where the periodic stacking of Bi bilayers can be seen. (**e**) A HAADF image of Bi$_{TRIG}$ (012) grain in a polycrystalline epilayer acquired along Si $[1\bar{1}0]$ projection. The central marked region is magnified, filtered (band-pass) and depicted in (**f**), where the puckered structures of Bi atoms along with a strong buckling between puckered atoms can be perceived. (**g**) A HAADF image of Bi$_{ORTH}$ (010) epilayer acquired at the cross-section along Si $[1\bar{1}0]$ projection. The domain is observed to be 2° in-plane rotated with respect to the substrate, which does not allow acquisition of atomically resolved images at the interface. The central highlighted region is magnified and depicted in (**h**), where the pseudo-cubic structure of Bi sub-lattice is evident.

Figure 9g represents a HAADF image acquired at the cross-section of a Bi$_{ORTH}$ epilayer along the Si $[1\bar{1}0]$ projection. An apparently relaxed and periodic stacking of the Bi monolayer ordered in a cubic-like structure can be witnessed in the image. An atomically sharp and clean interface between the substrate and the Bi$_{ORTH}$ epilayer is also evident. As established during XRD investigations, the unique alignment of the Bi$_{ORTH}$ crystals with a 45° in-plane offset with the Si (111) substrate facilitates the formation of a pseudo-cubic sub-lattice. A magnified HAADF image depicted in Figure 9h represents the Bi$_{CUB}$ structure, with the in-plane and the out-of-plane lattices measured to be 6.57 ± 0.02 Å and 6.44 ± 0.02 Å, respectively. The acquired values from STEM are in good approximation with XRD acquired lattices, depicted in Figure 8d–f.

8. Thickness-Dependent Phase Transformations

With such a thorough study of Bi epitaxial growth, most of the earlier introduced obscurities regarding nanofilm allotropes are addressed. However, one issue still remains unaddressed: the thickness-dependent phase transformation in Bi epilayers. As mentioned earlier, various reports have confirmed the existence of Bi$_{ORTH}$ phase during early stages of growth where the Bi$_{ORTH}$ phase is identified in the form of crystallites not only on Si (111) but also on Al$_2$O$_3$ (0001) and HOPG substrates [10,13,15,16,27,29,39]. According to these reports, the Bi$_{ORTH}$ phase is observed to be stable in ultra-thin films consisting of up to four

monolayers (4ML), approx. 1.3 nm thick. As soon as layer thickness increases, a transformation from Bi_{ORTH} into Bi_{TRIG} (001) phase is reported to initiate, which remains true if the layer thickness remains below 8–10 ML (approx. 3.5 nm). However, any film having a thickness > 3.5 nm is reported to crystallize only in the Bi_{TRIG} (001) phase. These observations are often supported by theoretical modelling and simulations [21,29,41]. The findings in this work mostly contradict the above-mentioned reports, as the epitaxial growths of the Bi_{TRIG} (001) and the Bi_{ORTH} phases are performed independently of each other.

However, before releasing a final statement, the dependency of phase transformation on the layer thickness is investigated, and the thickness-dependent controlled epitaxy of both phases, i.e., the Bi_{TRIG} (001) and the Bi_{ORTH} (010), is performed in a systematic manner. The growth parameters are adjusted to the optimum values for the Bi_{TRIG} (001), $(T_{sub}, R_{TF}) = (40\,°C, 22\,nm/h)$, and epilayers ranging in thickness from 2.2 nm to 13.5 nm are prepared. Figure 10 represents the XRD characterization of the Bi_{TRIG} (001) thickness series, where (a) depicts XRR curves, and (b) depicts the corresponding diffraction patterns. It is evident that all epilayers exhibit only the Bi_{TRIG} (001) phase, and no indication of phase duality is observed. The black-dotted line highlights a shift in the out-of-plane lattice constant due to the scaling effect. This effect has already been reported for GeTe [42]; however, it is not discussed here for Bi. As the focus of this work is on the thickness-dependent phase transformation, the investigation of the scaling effect within the same phase is outside the scope of this work. Nonetheless, the growth parameters are then adjusted to the Bi_{ORTH} optimum values, $(T_{sub}, R_{TF}) = (100\,°C, 32\,nm/h)$, and epilayers in thickness ranging from 1.6 nm to 13.6 nm are prepared. The results are summarized via symmetric RSMs around the Bi_{ORTH} (020) peak and are depicted in Figure 11.
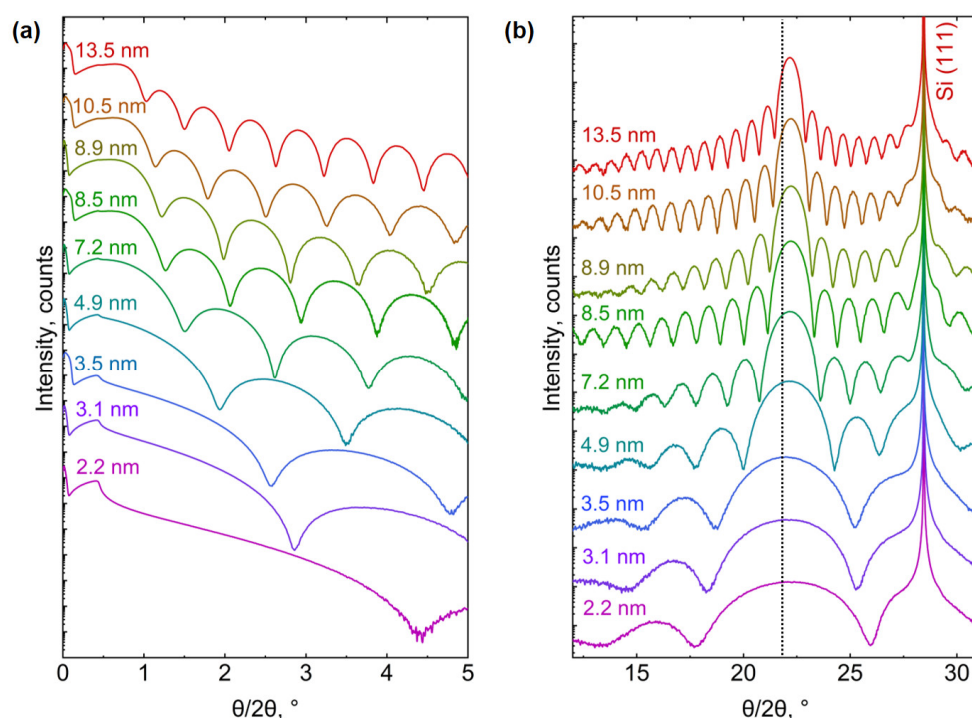

Figure 10. Thickness series of the Bi_{TRIG} (001) phase. (**a**) XRR-measured curves of epilayers ranging in thickness from 2.2 nm to 13.5 nm, whereas (**b**) depicts the corresponding diffraction patterns. The dotted black line in (**b**) indicates a slight shift in the out-of-plane lattice parameter due to thin-film effect.
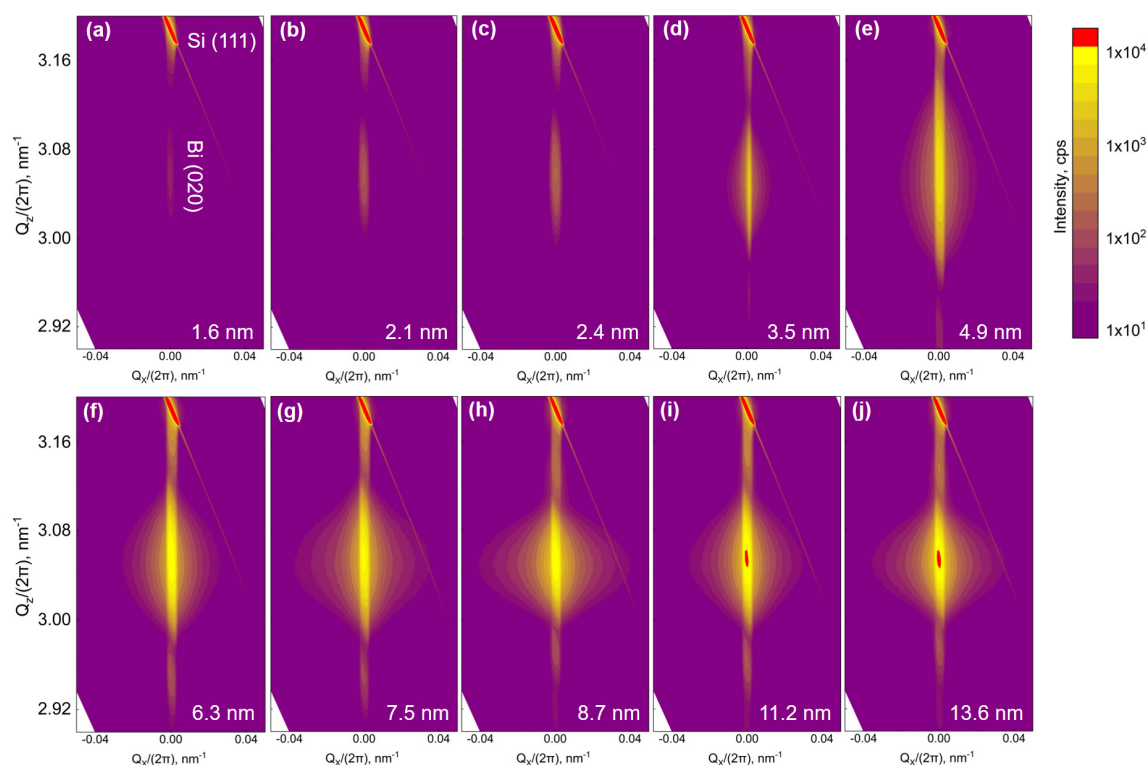
Figure 11. Thickness series of the Bi_{ORTH} (010) phase. The presence of a high-intensity Si (111) peak in vicinity of the Bi_{ORTH} (020) peak does not facilitate the analysis of thin films via diffraction pattern; however, it can be adopted as a reference in a symmetric RSM. Various symmetric RSMs of Bi_{ORTH} epilayers are acquired at the (020) peak, while the epilayer thickness is varied from (**a**) 1.6 nm to (**b**) 2.1 nm, (**c**) 2.4 nm, (**d**) 3.5 nm, (**e**) 4.9 nm, (**f**) 6.3 nm, (**g**) 7.5 nm, (**h**) 8.7 nm, (**i**) 11.2 nm and (**j**) 13.6 nm.

The presence of the Bi_{ORTH} (020) peak in layers having a thickness $\gg$ 3.5 nm is clear evidence that the Bi_{ORTH} epilayers can be grown phase-segregated and that layer thickness has no direct relation to phase transformation. Still, it is of critical importance to identify probable factors that may have led to the thickness-dependent phase transformation of Bi_{ORTH} in earlier-reported studies. The two key differences in this work compared to earlier reports are the substrate surface and the selection of growth parameters. (1) In this work, all growths are performed on Si (111) 1×1 conventional surfaces passivated by Bi-monolayers, whereas all earlier reports have adopted Si (111) $\sqrt{3} \times \sqrt{3} - \beta$ or 7×7 reconstructed surfaces that may have influenced the starting phase of Bi films. (2) For the first time, phase-dependent optimum growth parameters are evaluated and implemented in this work to affirm the phase purity of the growing epilayer The thickness-dependent phase transformation may be realized if similar growths are carried out with non-optimal parameters, i.e., in the "transformation zone" or at the zone boundary. However, it is just speculation until confirmed.

Though a thickness-dependent phase transformation in the Bi_{ORTH} epilayers is not realized, a continuous shift in the lattice parameters is observed. Figure 11 indicates only a slight change in the out-of-plane lattice depending on the epilayer thickness, whereas major changes are perceived in the in-plane structure of Bi_{ORTH}. It is observed that at low thicknesses, epilayers exhibit a relatively large difference between the in-plane lattice parameters, while the buckling height remains rather small, as witnessed in Figure 8a. With increasing thickness, the difference between in-plane lattice parameters decreases, whereas the buckling height increases, thus affirming the increasing strain in the epilayer, as depicted in Figure 8d. The observed trend of buckling height dependency on the Bi_{ORTH} layer thickness is summarized in Figure 12. Using linear interpolation, it is identified that

the black-phosphorus phase of Bi (Bi_{BP}) that exhibits zero-buckling can only be realized if the epilayer thickness remains below 1.32 nm. As the thinnest Bi_{ORTH} epilayer achieved in this work is only 1.63 nm thick, the requirements for realization of the Bi_{BP} phase are not met, and thus, only the Bi_{ORTH} phase is observed. The measured buckling values in Figure 12 also indicate that if such an ultra-thin epilayer is achieved, the probability of realizing the Bi_{BP} phase is high.
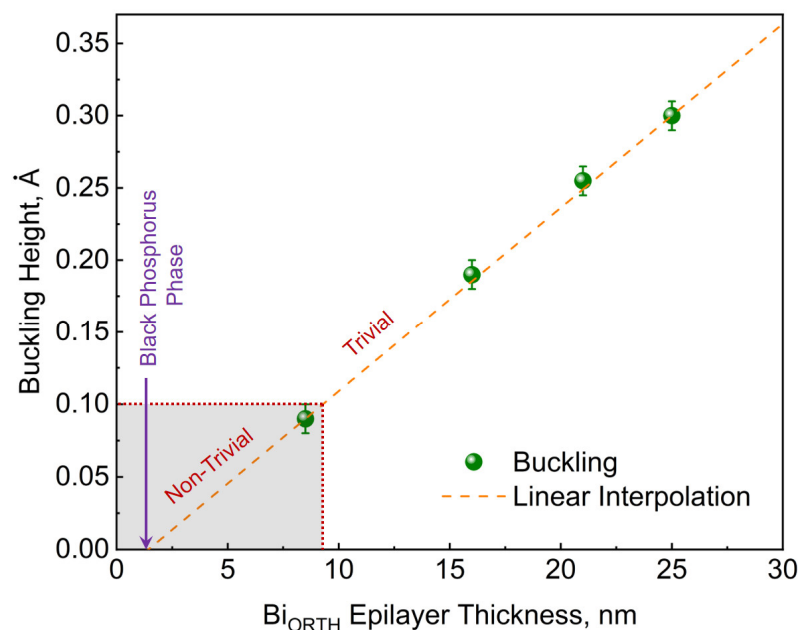

Figure 12. Buckling height vs. topology in the Bi_{ORTH} epilayers. Linear interpolation of thickness-dependent acquired values indicate that the buckling height in Bi_{ORTH} epilayers should reach zero, which would allow the realization of the black-phosphorus-like phase of Bi (Bi_{BP}). According to the theoretical model in [13], any Bi_{ORTH} epilayer hosting the buckling height ≤ 0.1 Å must exhibit topology, and thus, all Bi_{ORTH} epilayers with thickness ≤ 9 nm are predicted to exhibit non-trivial attributes.

Furthermore, the buckling height is reported to have a huge influence on the topological properties of Bi_{ORTH}. According to Lu et al., all epilayers with buckling height ≤ 0.1 Å exhibit non-trivial topology, whereas increasing buckling height transforms the epilayer into a trivial phase [13]. Based on this, all Bi_{ORTH} epilayers prepared in this work having a thickness ≤ 9 nm must exhibit non-trivial attributes, which was only true for approx. 1.3 nm thick epilayers in all earlier-reported studies. It facilitates the realization of Bi_{ORTH}-based quantum devices, as the achievement of fully coalesced 9 nm-thick epilayers is far less complex than 1.3 nm. The increasing buckling height in the epilayer indicates that after a certain thickness, the Bi_{ORTH} epilayer becomes unfavorable and will cross the limit of quantum confinement and transform into the Bi_{TRIG} (001) phase, just as reported in earlier studies. This hypothesis is confirmed with an attempt to grow a 45 nm-thick Bi_{ORTH} epilayer, which resulted in a polycrystalline film containing the Bi_{ORTH} and the Bi_{TRIG} (001) structures, confirming that the maximum stable thickness of the Bi_{ORTH} phase is somewhere between 30 nm (depicted in Figure 9) and 45 nm.

The groundwork for manufacturing nano-devices has now been laid with the successful phase-selective epitaxy of Bi-thin films. However, one must proceed with the utmost caution, as Bi oxidizes quickly when exposed to air. In the initial stages of oxidation, Bi forms a polycrystalline BiO_x layer, as depicted in Figure 9e. The polycrystalline nature of BiO_x makes it significantly challenging to remove during metallization, and access to a pristine epi-surface to realize atomically clean and sharp interface remains a challenge. A detailed and systematic study of surface oxidation in Bi thin films is performed; however,

it is not discussed here as it is outside the scope of this work. Furthermore, due to a low thermal stability, conventional fabrication techniques may degrade the crystal quality of Bi epilayers, which makes it even more challenging to realize functional quantum devices. An earlier-proposed platform with an on-chip stencil mask provides a way around the fabrication challenges [43], whereas the issue of surface oxidation can be addressed via in situ capping of the epitaxial surface with a passivation layer. Various topological insulator thin films are reported to have successfully achieved surface passivation using an electron beam-deposited thin film of stoichiometric Al_2O_3 [43–46]. In some circumstances, a 2 nm thermally evaporated film of elemental Al is adopted as passivation [47–52]. Al readily oxidizes and transforms into AlO_x when exposed to air, protecting the underlying surface from deterioration and aging. By combining phase-selective growth of Bi with an on-chip stencil mask [43] and in situ surface passivation, this study can be used to realize promising quantum devices for a variety of novel topological and neuromorphic applications.

9. Conclusions

In conclusion, we have demonstrated the high-quality growth of Bi thin films of various phases via molecular beam epitaxy on Si (111) 1×1 surfaces. First, the growth parameters for the trigonal phase, i.e., Bi_{TRIG} (001), were optimized to $T_{sub} = 40\ °C$ and $R_{TF} = 22\ nm/h$, yielding rocking curves as sharp as $53 \pm 10''$. By increasing the substrate temperature from $T_{sub} = 40\ °C$ to $95\ °C$, a structural transformation of the Bi epilayers into the orthorhombic phase Bi_{ORTH} (010) was observed. After optimizing the crystal quality of the Bi_{ORTH} (010) to a rocking curve value of $58 \pm 10''$, φ-scans of various growth series were performed to cast light on the dynamic transformation between the trigonal and orthorhombic Bi phases as a function of T_{sub} and R_{TF}. Strikingly, it was found that the six-fold symmetry of the twinned trigonal phase, i.e., Bi_{TRIG} (001), transforms partly into an intermediate phase before fully relaxing into the orthorhombic phase. The observed intermediate phase with its characteristic three-pointed peaks was identified as the Bi_{TRIG} (012) phase. As the out-of-plane lattices of Bi_{ORTH} (010) from Bi_{TRIG} (012) orientations are very similar, asymmetric RSMs were used to distinguish the intermediate from the orthorhombic phase. Next, the amount of buckling in phase-pure Bi_{ORTH} (010) thin films was investigated, as it was proposed that the degree of buckling determines the topological class the Bi crystal belongs to. It was found that the buckling height increases with the thickness of the epilayers. Unlike earlier reports, the maximum height of phase-pure Bi_{ORTH} (010) before transforming into Bi_{TRIG} (001) was found to be 30 nm, in contrast to the 1.3 nm value reported previously as the critical height. The enhanced maximum height observed in our study allows for the exploration of the topological phase in Bi_{ORTH} (010), which has been predicted to be present in films as thick as 9 nm. We attribute this key finding to the selection of the Si (111) 1×1 surface that we use for Bi epitaxy. Earlier studies used either Si (111) 7×7 or $\sqrt{3} \times \sqrt{3} - \beta$ reconstructions, which only allowed for the growth of non-coalesced crystallites of Bi_{ORTH} (010), which are not suitable for systematic integration into device circuitry. The 1×1 surface used here, however, allows for the phase-pure and thickness-independent growth of fully coalesced thin films of high-quality Bi_{ORTH} (010) up to 30 nm. These results pave the way to study and exploit the topological phases and phase transitions in Bi_{ORTH} (010) in future quantum devices.

Supplementary Materials: The following supporting information can be downloaded at: https://www.mdpi.com/article/10.3390/nano13142143/s1, Figure S1. XRD investigation of Bi_{TRIG} (012) epilayer via asymmetric RSMs probed at (a) (116), (b) (030), (c) $(\bar{3}18)$ and (d) $(\bar{3}\bar{1}4)$ peaks. Figure S2. XRD diffraction peaks map of Bi_{ORTH} (010) at $\varphi = 45°$. Figure S3. XRD diffraction peaks map of Bi_{CUB} along Si $[1\bar{1}0]$ projections. Figure S4. XRD diffraction peaks map of Bi_{CUB} along Si [211] projection. Figure S5. Evaluation of lattice parameters via measuring RSMs at Bi_{CUB} $(\bar{2}40)$ and Bi_{CUB} $(04\bar{2})$ peaks are 30° rotated domain. Figure S6. Evaluation of lattice parameters via measuring RSMs at Bi_{CUB} $(\bar{2}40)$ and Bi_{CUB} $(04\bar{2})$ peaks are 60° rotated domain. Figure S7. HAADF images of Bi_{TRIG} (001), Bi_{TRIG} (012) and Bi_{ORTH} (010) epilayers confirming the large grain sizes and high crystal quality of the epilayers. Figure S8. HAADF images of Bi_{TRIG} (001) epilayers along Si [211] projection.

Figure S9. HAADF and bright field images indicating the effect of image acquisition time on the Bi_{TRIG} (001) epilayers. The average acquisition time in (b) is higher than (a). The damaged regions in (b) are the confirmation of Bi instability under elongated exposure. Figure S10. Sets of HAADF and bright field images representing the continually increasing structural damage of Bi epilayer with increasing illumination time under the electron beam. The interface between Bi and Si is witnessed to be the most affected region. The acquisition time in all images remains similar.

References

1. Koroteev, Y.M.; Bihlmayer, G.; Gayone, J.E.; Chulkov, E.V.; Blügel, S.; Echenique, P.M.; Hofmann, P. Strong spin-orbit splitting on bi surfaces. *Phys. Rev. Lett.* **2004**, *93*, 046403. [CrossRef] [PubMed]
2. Kurpas, M.; Faria Junior, P.E.; Gmitra, M.; Fabian, J. Spin-orbit coupling in elemental two-dimensional materials. *Phys. Rev. B* **2019**, *100*, 125422. [CrossRef]
3. Zhang, H.; Liu, C.-X.; Qi, X.-L.; Dai, X.; Fang, Z.; Zhang, S.-C. Topological insulators in bi2se3, bi2te3 and sb2te3 with a single dirac cone on the surface. *Nat. Phys.* **2009**, *5*, 438–442. [CrossRef]
4. Fu, L.; Kane, C.L. Topological insulators with inversion symmetry. *Phys. Rev. B* **2007**, *76*, 045302. [CrossRef]
5. Jalil, A.R.; Schüffelgen, P.; Valencia, H.; Schleenvoigt, M.; Ringkamp, C.; Mussler, G.; Luysberg, M.; Mayer, J.; Grützmacher, D. Selective area epitaxy of quasi-1-dimensional topological nanostructures and networks. *Nanomaterials* **2023**, *13*, 354. [CrossRef] [PubMed]
6. Jalil, A.R. *Engineering Topological Superlattices and Their Epitaxial Integration in Selectively Grown Hybrid Nanostructures via Mbe*; Halbleiter-Nanoelektronik; RWTH Aachen University: Aachen, Germany, 2022; p. 309.
7. Aggarwal, L.; Zhu, P.; Hughes, T.L.; Madhavan, V. Evidence for higher order topology in bi and $bi_{0.92}sb_{0.08}$. *Nat. Commun.* **2021**, *12*, 4420. [CrossRef]
8. Schindler, F.; Wang, Z.; Vergniory, M.G.; Cook, A.M.; Murani, A.; Sengupta, S.; Kasumov, A.Y.; Deblock, R.; Jeon, S.; Drozdov, I.; et al. Higher-order topology in bismuth. *Nat. Phys.* **2018**, *14*, 918–924. [CrossRef]
9. Reis, F.; Li, G.; Dudy, L.; Bauernfeind, M.; Glass, S.; Hanke, W.; Thomale, R.; Schäfer, J.; Claessen, R. Bismuthene on a sic substrate: A candidate for a high-temperature quantum spin hall material. *Science* **2017**, *357*, 287–290. [CrossRef]
10. Gou, J.; Kong, L.; He, X.; Huang, Y.L.; Sun, J.; Meng, S.; Wu, K.; Chen, L.; Wee, A.T.S. The effect of moiré superstructures on topological edge states in twisted bismuthene homojunctions. *Sci. Adv.* **2020**, *6*, eaba2773. [CrossRef]
11. Drozdov, I.K.; Alexandradinata, A.; Jeon, S.; Nadj-Perge, S.; Ji, H.; Cava, R.J.; Andrei Bernevig, B.; Yazdani, A. One-dimensional topological edge states of bismuth bilayers. *Nat. Phys.* **2014**, *10*, 664–669. [CrossRef]

12. Takayama, A.; Sato, T.; Souma, S.; Oguchi, T.; Takahashi, T. One-dimensional edge states with giant spin splitting in a bismuth thin film. *Phys. Rev. Lett.* **2015**, *114*, 066402. [CrossRef]

13. Lu, Y.; Xu, W.; Zeng, M.; Yao, G.; Shen, L.; Yang, M.; Luo, Z.; Pan, F.; Wu, K.; Das, T.; et al. Topological properties determined by atomic buckling in self-assembled ultrathin bi(110). *Nano Lett.* **2015**, *15*, 80–87. [CrossRef] [PubMed]

14. Inbar, H.S.; Zubair, M.; Dong, J.T.; Engel, A.N.; Dempsey, C.P.; Chang, Y.H.; Nishihaya, S.; Khalid, S.; Fedorov, A.V.; Janotti, A. Inversion symmetry breaking in epitaxial ultrathin bi(111) films. *arXiv* **2023**, arXiv:2302.00803.

15. Gou, J.; Bai, H.; Zhang, X.; Huang, Y.L.; Duan, S.; Ariando, A.; Yang, S.A.; Chen, L.; Lu, Y.; Wee, A.T.S. Two-dimensional ferroelectricity in a single-element bismuth monolayer. *Nature* **2023**, *617*, 67–72. [CrossRef]

16. Jankowski, M.; Kamiński, D.; Vergeer, K.; Mirolo, M.; Carla, F.; Rijnders, G.; Bollmann, T.R.J. Controlling the growth of bi(110) and bi(111) films on an insulating substrate. *Nanotechnology* **2017**, *28*, 155602. [CrossRef] [PubMed]

17. Wang, N.; Dai, Y.-X.; Wang, T.-L.; Yang, H.-Z.; Qi, Y. Investigation of growth characteristics and semimetal–semiconductor transition of polycrystalline bismuth thin films. *IUCrJ* **2020**, *7*, 49–57. [CrossRef] [PubMed]

18. Jiang, Z.; Soghomonian, V.; Heremans, J.J. Carrier properties of bi(111) grown on mica and si(111). *Phys. Rev. Mater.* **2022**, *6*, 095003. [CrossRef]

19. Kokubo, I.; Yoshiike, Y.; Nakatsuji, K.; Hirayama, H. Ultrathin bi(110) films on si(111)$\sqrt{3} \times \sqrt{3}$−b substrates. *Phys. Rev. B* **2015**, *91*, 075429. [CrossRef]

20. Yaginuma, S.; Nagao, T.; Sadowski, J.T.; Saito, M.; Nagaoka, K.; Fujikawa, Y.; Sakurai, T.; Nakayama, T. Origin of flat morphology and high crystallinity of ultrathin bismuth films. *Surf. Sci.* **2007**, *601*, 3593–3600. [CrossRef]

21. Nagao, T.; Sadowski, J.T.; Saito, M.; Yaginuma, S.; Fujikawa, Y.; Kogure, T.; Ohno, T.; Hasegawa, Y.; Hasegawa, S.; Sakurai, T. Nanofilm allotrope and phase transformation of ultrathin bi film on si(111)—7 × 7. *Phys. Rev. Lett.* **2004**, *93*, 105501. [CrossRef]

22. Kammler, M.; Horn-von Hoegen, M. Low energy electron diffraction of epitaxial growth of bismuth on si(111). *Surf. Sci.* **2005**, *576*, 56–60. [CrossRef]

23. Hirahara, T.; Nagao, T.; Matsuda, I.; Bihlmayer, G.; Chulkov, E.V.; Koroteev, Y.M.; Hasegawa, S. Quantum well states in ultrathin bi films: Angle-resolved photoemission spectroscopy and first-principles calculations study. *Phys. Rev. B* **2007**, *75*, 035422. [CrossRef]

24. Takayama, A.; Sato, T.; Souma, S.; Oguchi, T.; Takahashi, T. Tunable spin polarization in bismuth ultrathin film on si(111). *Nano Lett.* **2012**, *12*, 1776–1779. [CrossRef]

25. Yaji, K.; Kuroda, K.; Toyohisa, S.; Harasawa, A.; Ishida, Y.; Watanabe, S.; Chen, C.; Kobayashi, K.; Komori, F.; Shin, S. Spin-dependent quantum interference in photoemission process from spin-orbit coupled states. *Nat. Commun.* **2017**, *8*, 14588. [CrossRef] [PubMed]

26. Stanionytė, S.; Malinauskas, T.; Niaura, G.; Skapas, M.; Devenson, J.; Krotkus, A. The crystalline structure of thin bismuth layers grown on silicon(111) substrates. *Materials* **2022**, *15*, 4847. [CrossRef] [PubMed]

27. Hofmann, P. The surfaces of bismuth: Structural and electronic properties. *Prog. Surf. Sci.* **2006**, *81*, 191–245. [CrossRef]

28. Bollmann, T.R.J.; Jankowski, M. Kinetics and the crystallographic structure of bismuth during liquefaction and solidification on an insulating substrate. *Surf. Sci.* **2022**, *723*, 122106. [CrossRef]

29. Lyu, Y.; Daneshmandi, S.; Huyan, S.; Chu, C. Flexible atomic buckling and homogeneous edge states in few-layer bi(110) films. *Nano Res.* **2022**, *15*, 2374–2381. [CrossRef]

30. Hoffman, C.A.; Meyer, J.R.; Bartoli, F.J.; Di Venere, A.; Yi, X.J.; Hou, C.L.; Wang, H.C.; Ketterson, J.B.; Wong, G.K. Semimetal-to-semiconductor transition in bismuth thin films. *Phys. Rev. B* **1993**, *48*, 11431–11434. [CrossRef]

31. Xiao, S.; Wei, D.; Jin, X. Bi(111) thin film with insulating interior but metallic surfaces. *Phys. Rev. Lett.* **2012**, *109*, 166805. [CrossRef]

32. Gity, F.; Ansari, L.; Lanius, M.; Schüffelgen, P.; Mussler, G.; Grützmacher, D.; Greer, J.C. Reinventing solid state electronics: Harnessing quantum confinement in bismuth thin films. *Appl. Phys. Lett.* **2017**, *110*, 093111. [CrossRef]

33. Pilidi, A.; Tzanis, A.; Helm, T.; Arfanis, M.; Falaras, P.; Speliotis, T. Nanometer-thick bismuth nanocrystal films for sensoric applications. *ACS Appl. Nano Mater.* **2020**, *3*, 9669–9678. [CrossRef]

34. Handegård, Ø.S.; Kitajima, M.; Nagao, T. Laser-induced structural disordering and optical phase change in semimetal bismuth observed by raman microscopy. *Appl. Surf. Sci.* **2019**, *491*, 675–681. [CrossRef]

35. Krogstrup, P.; Ziino, N.L.B.; Chang, W.; Albrecht, S.M.; Madsen, M.H.; Johnson, E.; Nygård, J.; Marcus, C.M.; Jespersen, T.S. Epitaxy of semiconductor–superconductor nanowires. *Nat. Mater.* **2015**, *14*, 400–406. [CrossRef] [PubMed]

36. Pendharkar, M.; Zhang, B.; Wu, H.; Zarassi, A.; Zhang, P.; Dempsey, C.P.; Lee, J.S.; Harrington, S.D.; Badawy, G.; Gazibegovic, S.; et al. Parity-preserving and magnetic field–resilient superconductivity in insb nanowires with sn shells. *Science* **2021**, *372*, 508–511. [CrossRef]

37. Fujita, K.; Kusumi, Y.; Ichikawa, M. Nucleation along step edges during si epitaxial growth on the si(111) surface observed by stm. *Surf. Sci.* **1997**, *380*, 66–74. [CrossRef]

38. Kowalczyk, P.J.; Mahapatra, O.; McCarthy, D.N.; Kozlowski, W.; Klusek, Z.; Brown, S.A. Stm and xps investigations of bismuth islands on hopg. *Surf. Sci.* **2011**, *605*, 659–667. [CrossRef]

39. Scott, S.A.; Kral, M.V.; Brown, S.A. A crystallographic orientation transition and early stage growth characteristics of thin bi films on hopg. *Surf. Sci.* **2005**, *587*, 175–184. [CrossRef]

40. Zhou, H.; Wu, L.; Wang, H.-Q.; Zheng, J.-C.; Zhang, L.; Kisslinger, K.; Li, Y.; Wang, Z.; Cheng, H.; Ke, S.; et al. Interfaces between hexagonal and cubic oxides and their structure alternatives. *Nat. Commun.* **2017**, *8*, 1474. [CrossRef]

41. Koroteev, Y.M.; Bihlmayer, G.; Chulkov, E.V.; Blügel, S. First-principles investigation of structural and electronic properties of ultrathin bi films. *Phys. Rev. B* **2008**, *77*, 045428. [CrossRef]

42. Kerres, P.; Zhou, Y.; Vaishnav, H.; Raghuwanshi, M.; Wang, J.; Häser, M.; Pohlmann, M.; Cheng, Y.; Schön, C.-F.; Jansen, T.; et al. Scaling and confinement in ultrathin chalcogenide films as exemplified by gete. *Small* **2022**, *18*, 2201753. [CrossRef]

43. Schüffelgen, P.; Rosenbach, D.; Li, C.; Schmitt, T.W.; Schleenvoigt, M.; Jalil, A.R.; Schmitt, S.; Kölzer, J.; Wang, M.; Bennemann, B.; et al. Selective area growth and stencil lithography for in situ fabricated quantum devices. *Nat. Nanotechnol.* **2019**, *14*, 825–831. [CrossRef]

44. Kölzer, J.; Jalil, A.R.; Rosenbach, D.; Arndt, L.; Mussler, G.; Schüffelgen, P.; Grützmacher, D.; Lüth, H.; Schäpers, T. Supercurrent in bi$_4$te$_3$ topological material-based three-terminal junctions. *Nanomaterials* **2023**, *13*, 293. [CrossRef] [PubMed]

45. Schmitt, T.W.; Connolly, M.R.; Schleenvoigt, M.; Liu, C.; Kennedy, O.; Chávez-Garcia, J.M.; Jalil, A.R.; Bennemann, B.; Trellenkamp, S.; Lentz, F.; et al. Integration of topological insulator josephson junctions in superconducting qubit circuits. *Nano Lett.* **2022**, *22*, 2595–2602. [CrossRef]

46. Rosenbach, D.; Jalil, A.R.; Schmitt, T.W.; Bennemann, B.; Mussler, G.; Schüffelgen, P.; Grützmacher, D.; Schäpers, T. Ballistic surface channels in fully in situ defined Bi$_4$Te$_3$ josephson junctions with aluminum contacts. *arXiv* **2023**, arXiv:2301.03968.

47. Rosenbach, D.; Oellers, N.; Jalil, A.R.; Mikulics, M.; Kölzer, J.; Zimmermann, E.; Mussler, G.; Bunte, S.; Grützmacher, D.; Lüth, H.; et al. Quantum transport in topological surface states of selectively grown bi$_2$te$_3$ nanoribbons. *Adv. Electron. Mater.* **2020**, *6*, 2000205. [CrossRef]

48. Kölzer, J.; Rosenbach, D.; Weyrich, C.; Schmitt, T.W.; Schleenvoigt, M.; Jalil, A.R.; Schüffelgen, P.; Mussler, G.; Sacksteder, V.E., IV; Grützmacher, D.; et al. Phase-coherent loops in selectively-grown topological insulator nanoribbons. *Nanotechnology* **2020**, *31*, 325001. [CrossRef] [PubMed]

49. Kölzer, J.; Moors, K.; Jalil, A.R.; Zimmermann, E.; Rosenbach, D.; Kibkalo, L.; Schüffelgen, P.; Mussler, G.; Grützmacher, D.; Schmidt, T.L. In-plane magnetic field-driven symmetry breaking in topological insulator-based three-terminal junctions. *arXiv* **2020**, arXiv:2012.15118. [CrossRef]

50. Schäpers, T.; Weyrich, C.; Rosenbach, D.; Kölzer, J.; Schmitt, T.; Schüffelgen, P.; Mussler, G.; Schleenvoigt, M.; Jalil, A.R.; Lüth, H. *Phase-Coherent Transport in Topological Insulator Nanocolumns and Nanoribbons*; Spintronics XI, 2018; International Society for Optics and Photonics: Bellingham, WA, USA, 2018; p. 107320V.

51. Rosenbach, D.; Moors, K.; Jalil, A.R.; Kölzer, J.; Zimmermann, E.; Schubert, J.; Karimzadah, S.; Mussler, G.; Schüffelgen, P.; Grützmacher, D. Gate-induced decoupling of surface and bulk state properties in selectively-deposited bi$_2$te$_3$ nanoribbons. *SciPost Phys. Core* **2022**, *5*, 17. [CrossRef]

52. Behner, G.; Jalil, A.R.; Heffels, D.; Kölzer, J.; Moors, K.; Mertens, J.; Zimmermann, E.; Mussler, G.; Schüffelgen, P.; Lüth, H.; et al. Aharonov-bohm interference and phase-coherent surface-state transport in topological insulator rings. *Nano Lett.* **2023**, *23*, 1–5. [CrossRef] [PubMed]